Theses and Dissertations   1. Thesis and Dissertation Collection, all items

2019-06

MINIMUM ELECTRICAL ENERGY SPACECRAFT MANEUVERS: THEORY AND EXPERIMENTS

Culton, Eryn A.

Monterey, CA; Naval Postgraduate School

http://hdl.handle.net/10945/62701

NAVAL
POSTGRADUATE
SCHOOL

MONTEREY, CALIFORNIA

THESIS

**MINIMUM ELECTRICAL ENERGY SPACECRAFT
MANEUVERS: THEORY AND EXPERIMENTS**

by

Eryn A. Culton

June 2019

Thesis Advisor:	Mark Karpenko
Second Reader:	Harleigh Marsh

THIS PAGE INTENTIONALLY LEFT BLANK

		Form Approved OMB No. 0704-0188
REPORT DOCUMENTATION PAGE		

Public reporting burden for this collection of information is estimated to average 1 hour per response, including the time for reviewing instruction, searching existing data sources, gathering and maintaining the data needed, and completing and reviewing the collection of information. Send comments regarding this burden estimate or any other aspect of this collection of information, including suggestions for reducing this burden, to Washington headquarters Services, Directorate for Information Operations and Reports, 1215 Jefferson Davis Highway, Suite 1204, Arlington, VA 22202-4302, and to the Office of Management and Budget, Paperwork Reduction Project (0704-0188) Washington, DC 20503.

1. AGENCY USE ONLY (Leave blank)	2. REPORT DATE June 2019	3. REPORT TYPE AND DATES COVERED Master's thesis

4. TITLE AND SUBTITLE MINIMUM ELECTRICAL ENERGY SPACECRAFT MANEUVERS: THEORY AND EXPERIMENTS		5. FUNDING NUMBERS
6. AUTHOR(S) Eryn A. Culton		

7. PERFORMING ORGANIZATION NAME(S) AND ADDRESS(ES) Naval Postgraduate School Monterey, CA 93943-5000	8. PERFORMING ORGANIZATION REPORT NUMBER
9. SPONSORING / MONITORING AGENCY NAME(S) AND ADDRESS(ES) N/A	10. SPONSORING / MONITORING AGENCY REPORT NUMBER

11. SUPPLEMENTARY NOTES The views expressed in this thesis are those of the author and do not reflect the official policy or position of the Department of Defense or the U.S. Government.

12a. DISTRIBUTION / AVAILABILITY STATEMENT Approved for public release. Distribution is unlimited.	12b. DISTRIBUTION CODE A

13. ABSTRACT (maximum 200 words)

Reaction wheels are popular satellite attitude control actuators that have been the subject of years of research. Recently, optimal control theory was applied to discover a new reaction wheel control algorithm that steers the spacecraft along an alternate path, minimizing power draw for a system of redundant (four or more) reaction wheels while completing a shortest-time maneuver. This thesis characterizes the energy draw of a particular slewing maneuver using both a conventional attitude maneuver trajectory and trajectories derived using the new concept. In particular, a minimum energy optimal control problem is solved to find efficient energy profiles for a realistic reaction wheel spacecraft attitude control system. These profiles build a maneuver cost tradespace, validating the nonlinear relationship between electrical energy consumption and maneuver duration. To bridge the gap between theory and practice, an experiment is also implemented to test the solutions involving a set of reaction wheels to measure power consumption. Ultimately, an optimal maneuver operating envelope is created and the power model is verified to accurately characterize the power draw of a momentum exchange attitude control system.

14. SUBJECT TERMS energy efficient, attitude control, Optimal Control Theory, reaction wheel spacecraft			15. NUMBER OF PAGES 101
			16. PRICE CODE

17. SECURITY CLASSIFICATION OF REPORT Unclassified	18. SECURITY CLASSIFICATION OF THIS PAGE Unclassified	19. SECURITY CLASSIFICATION OF ABSTRACT Unclassified	20. LIMITATION OF ABSTRACT UU

THIS PAGE INTENTIONALLY LEFT BLANK

**MINIMUM ELECTRICAL ENERGY SPACECRAFT MANEUVERS:
THEORY AND EXPERIMENTS**

Eryn A. Culton
Ensign, United States Navy
BS, U.S. Naval Academy, 2018

Submitted in partial fulfillment of the
requirements for the degree of

MASTER OF SCIENCE IN ASTRONAUTICAL ENGINEERING

from the

**NAVAL POSTGRADUATE SCHOOL
June 2019**

Approved by: Mark Karpenko
                 Advisor

                 Harleigh Marsh
                 Second Reader

                 Garth V. Hobson
                 Chair, Department of Mechanical and Aerospace Engineering

THIS PAGE INTENTIONALLY LEFT BLANK

ABSTRACT

Reaction wheels are popular satellite attitude control actuators that have been the subject of years of research. Recently, optimal control theory was applied to discover a new reaction wheel control algorithm that steers the spacecraft along an alternate path, minimizing power draw for a system of redundant (four or more) reaction wheels while completing a shortest-time maneuver. This thesis characterizes the energy draw of a particular slewing maneuver using both a conventional attitude maneuver trajectory and trajectories derived using the new concept. In particular, a minimum energy optimal control problem is solved to find efficient energy profiles for a realistic reaction wheel spacecraft attitude control system. These profiles build a maneuver cost tradespace, validating the nonlinear relationship between electrical energy consumption and maneuver duration. To bridge the gap between theory and practice, an experiment is also implemented to test the solutions involving a set of reaction wheels to measure power consumption. Ultimately, an optimal maneuver operating envelope is created and the power model is verified to accurately characterize the power draw of a momentum exchange attitude control system.

THIS PAGE INTENTIONALLY LEFT BLANK

TABLE OF CONTENTS

THIS PAGE INTENTIONALLY LEFT BLANK

LIST OF FIGURES

LIST OF TABLES

THIS PAGE INTENTIONALLY LEFT BLANK

ACKNOWLEDGMENTS

THIS PAGE INTENTIONALLY LEFT BLANK

I. INTRODUCTION

Many spacecraft require the ability to maneuver and point precisely to execute their designed mission. For some spacecraft, changing the attitude quickly is desired in order to improve overall mission data return: Intelligence satellites need to be able to point quickly to commanded locations to gather critical intelligence, while scientific mission-oriented spacecraft need this same quick response to catch phenomena and increase communications windows in order to downlink a larger amount of collected data. Extending data collection and downlink windows increases the payload and communication subsystems' draw on the electrical power system. To provide this extra power, conserving electrical energy during other operations, including attitude control maneuvers, is quite desirable and may even be required [1, 2, 3]. Finding attitude pointing maneuvers that conserve electrical energy while also reducing slew time could provide spacecraft a larger power reserve, allowing for more, potentially longer, data collection periods.

Spacecraft can move with six degrees of freedom (DOF): three translational and three rotational. Although propulsive systems are commonly used to control the three translational DOF, many options for actuators can be used to control a spacecraft's rotational attitude. Reaction wheels are popular for attitude control of all sizes of spacecraft. Using reaction wheels, attitude is controlled via the conservation of angular momentum. Just like in translational motion, there exist multiple paths to travel from an initial to a final orientation in rotational space. In order to choose one particular path out of many, a cost or merit functional can be introduced in order to rank each path. Common metrics within spacecraft attitude control systems include distance, time, and fuel consumption/electrical energy use. To find an attitude maneuver that minimizes a given cost, optimal control theory can be applied. Optimal control theory finds a trajectory that minimizes a defined cost subject to a model of the rotational dynamics and desired boundary conditions [4]. Relating to spacecraft attitude control, optimal control theory has been used to find optimal attitude maneuvers that minimize time or electrical energy while considering the state and control constraints characteristic of a particular spacecraft system.

Although optimal control theory has been applied extensively in the attitude control community, the conventional attitude maneuver remains a simple minimum distance maneuver, also referred to as an Eigenaxis maneuver [5, 6, 7, 8]. Eigenaxis maneuvers were originally thought to be minimum time maneuvers. However, Eigenaxis maneuvers have generally been shown to not be time optimal maneuvers [9]. Reference [9] used then new advances in pseudospectral optimal control theory to find minimum time maneuvers for asymmetric, rigid body spacecraft, showing that minimum time maneuvers actually follow a non-intuitive path by rotating the spacecraft about multiple axes simultaneously instead of following the shortest path as defined by a rotation about a single axis. Although these minimum time maneuvers might take the least amount of time, they can potentially be expensive in respect to fuel/electrical energy consumption [3].

Electrical energy consumption has been modeled many different ways in spacecraft attitude control. Reference [10] uses a quadratic cost of a sum of applied torques squared to represent electrical energy as the cost to find a minimum energy attitude maneuver for an asymmetric, rigid body spacecraft with a non-redundant reaction wheel attitude control system. Although the sum of applied torques minimizes the magnitude of electrical current demanded by the attitude control system, this approach does not model how much electrical energy is actually used. Thus, the cost does not reflect the attitude control system's demand on the electrical power subsystem. References [2], [3], [11] and [12] attempt to remedy this issue by deriving a more detailed equation for momentum exchange devices' electrical energy consumption that takes various energy losses into account including copper loss and friction loss. Reference [3] used this detailed electrical energy model as a cost functional to establish the relation between maneuver time and energy for a reaction wheel spacecraft and shows that this relationship is nonlinear and inversely related. Using these relationships, [3] established the existence of a tradespace between on and off Eigenaxis maneuvering.

The purpose of this thesis is to further explore the energy requirements for of reaction wheel slews by characterizing the energy draw of slew maneuvers through experimental validation. Conventional attitude maneuvers are compared to a) a minimum electrical energy maneuver and b) a reduced time maneuver. Both of these optimal

maneuvers are derived using optimal control theory [4] for a system of redundant reaction wheels. A spacecraft model based off of NASA's Lunar Reconnaissance Orbiter (LRO) is used as an example of a practical spacecraft system. This thesis constructs an operating envelope which will be shown to follow the nonlinear electrical energy versus time relationship defined in [3] using the Eigenaxis maneuver cost as a baseline. The resulting envelope can be used for mission operations for slew planning to balance maneuver time against energy requirements. To bridge the gap between theory and practice, an experiment will be implemented to validate the power model that uses a set of reaction wheels to measure power consumption in the laboratory.

A.   THESIS OBJECTIVES AND SCOPE

Attitude maneuvers for a given set of boundary conditions will be found, tested, and compared within this thesis. The first maneuver is the standard Eigenaxis maneuver; it is a minimum distance maneuver that rotates the spacecraft about a single, fixed axis as defined by the maneuver's initial and final attitudes. The second maneuver will characterize the minimum amount of electrical energy needed to complete the same maneuver over the time duration of the Eigenaxis maneuver. That is, given the same boundary conditions, this solution will complete the maneuver in the same time as the Eigenaxis maneuver while using the least electrical energy. The third maneuver characterizes a reduced time maneuver that uses the same electrical energy consumption as an Eigenaxis maneuver, but does not enforce Eigenaxis maneuvering (resulting in a faster maneuver). These three maneuvers serve as corner cases, creating an operating envelope to find the slew time versus electrical energy tradespace. Once these three maneuvers are computationally obtained, they will be implemented on a testbed of redundant reaction wheels in the laboratory where empirical electrical energy use data will be collected in order to confirm the practicality of the approach.

B.   THESIS LAYOUT

This thesis will begin by introducing the dynamical model of a spacecraft to be used within this research in Chapter II. The standard Eigenaxis maneuver will be constructed in Chapter III and its time and power characteristics evaluated. Chapter IV builds the problem

formulation for the minimum electrical energy maneuver before developing its necessary conditions for optimality and obtaining a numerical solution. Chapter IV continues, vetting the numerical solution against the necessary conditions and concluding it is, in fact, an optimal maneuver solution. Chapter V does the same as Chapter IV but for the reduced time maneuver. Chapter VI describes the physical testbed used to collect empirical data along with the test procedures used before presenting the collected data. Finally, Chapter VII will include a summary of the completed research along with the concluding remarks and ideas for future work on this subject.

II.   SPACECRAFT AND REACTION WHEEL MODEL

Chapter II defines the dynamical model of the spacecraft and reaction wheel systems considered within this thesis. Optimal control theory can then be applied to the spacecraft attitude control system. The spacecraft and reaction wheel attitude control system models in this thesis are based off of the LRO as an example of a practical spacecraft system. Any remaining undefined parameters for the reaction wheel system will be modeled after a set of reaction wheels present in the Naval Postgraduate School's Control & Optimization Laboratory.

A.   NONLINEAR DYNAMICAL MODEL

Before outlining a particular attitude control system, the dynamics of general momentum exchange attitude control systems must be understood. Reaction wheels alter spacecraft attitude as a result of the conservation of angular momentum. The total spacecraft momentum can be represented as two terms, written in the body frame as Equation (1.1) [11].

$$\boldsymbol{H} = {}^{B}\boldsymbol{H}_{s/c} + {}^{B}\boldsymbol{H}_{rw} \tag{1.1}$$

Within Equation (1.1), ${}^{B}\boldsymbol{H}_{s/c}$ is the spacecraft angular momentum in the body frame and can be represented as Equation (1.2) while ${}^{B}\boldsymbol{H}_{rw}$ is the angular momentum of the reaction wheel array in the body frame and can be written as Equation (1.3).

$$ {}^{B}\boldsymbol{H}_{s/c} = \boldsymbol{J}\boldsymbol{\omega} \tag{1.2}$$

$$ {}^{B}\boldsymbol{H}_{rw} = \boldsymbol{Z}\boldsymbol{h}_{rw} = \boldsymbol{Z}\boldsymbol{J}_{w}\boldsymbol{\Omega} \tag{1.3}$$

where $\boldsymbol{J}$ and $\boldsymbol{J}_{w}$ are the spacecraft inertia tensor and reaction wheel rotational inertia, respectively, $\boldsymbol{\omega}$ and $\boldsymbol{\Omega}$ are the spacecraft body rotation rate and the reaction wheel rotation rate vector, and $\boldsymbol{Z}$ is the reaction wheel alignment matrix [11].

With the spacecraft body and reaction wheel momentum terms defined, the time rate of change of both terms can be written as Equation (1.4) and Equation (1.5).

$$^{B}\dot{\boldsymbol{H}}_{s/c} = \boldsymbol{J}\dot{\boldsymbol{\omega}} + \boldsymbol{\omega} \times \boldsymbol{J}\boldsymbol{\omega} \tag{1.4}$$

$$^{B}\dot{\boldsymbol{H}}_{rw} = \boldsymbol{Z}\boldsymbol{\tau} + \boldsymbol{\omega} \times \boldsymbol{Z}J_{w}\boldsymbol{\Omega} \tag{1.5}$$

where $\boldsymbol{\tau}$ is the control torque applied by the reaction wheels. The control torque is related to the reaction wheel acceleration as given by Equation (1.6) [11].

$$\boldsymbol{\tau} = J_{w}\dot{\boldsymbol{\Omega}} \tag{1.6}$$

Assuming no external disturbance torques are applied to the spacecraft system, the time rate of change of the spacecraft's angular momentum must be zero by the conservation of angular momentum [11]. This relationship is represented in Equation (1.7).

$$^{B}\dot{\boldsymbol{H}}_{s/c} + {}^{B}\dot{\boldsymbol{H}}_{rw} = 0 \tag{1.7}$$

Using Equation (1.4) and Equation (1.5) in Equation (1.7) and rearranging gives Equation (1.8).

$$\boldsymbol{J}\dot{\boldsymbol{\omega}} = -\boldsymbol{Z}\boldsymbol{\tau} - \boldsymbol{\omega} \times (\boldsymbol{J}\boldsymbol{\omega} + \boldsymbol{Z}J_{w}\boldsymbol{\Omega}) \tag{1.8}$$

Rearranging Equations (1.6) and (1.8) provides two equations describing the rotational dynamics of a redundant reaction wheel attitude control system. These relations are represented in Equations (1.9) and (1.10) and will be used as part of the dynamical model in this thesis.

$$\dot{\boldsymbol{\omega}} = \boldsymbol{J}^{-1}(-\boldsymbol{\omega} \times (\boldsymbol{J}\boldsymbol{\omega} + \boldsymbol{Z}J_{w}\boldsymbol{\Omega}) - \boldsymbol{Z}\boldsymbol{\tau}) \tag{1.9}$$

$$\dot{\boldsymbol{\Omega}} = \frac{\boldsymbol{\tau}}{J_{w}} \tag{1.10}$$

Lastly, to fully describe a spacecraft's attitude throughout a slewing maneuver, the attitude kinematics must be defined. Quaternions are used within this thesis to parameterize the spacecraft's attitude and are calculated as shown in Equation (1.11) [8, 13].

$$\boldsymbol{q} = [e_1 \sin(\Phi/2), e_2 \sin(\Phi/2), e_3 \sin(\Phi/2), \cos(\Phi/2)]^T \tag{1.11}$$

where $\hat{\boldsymbol{e}} = [e_1, e_2, e_3]^T$ is the Eigen axis and Φ is the rotation about the Eigen axis.

The time rate of change of the attitude quaternions can be represented as Equation (1.12) [8, 13].

$$\dot{q} = \frac{1}{2} Q(\omega) q \tag{1.12}$$

where $Q(\omega)$ is a skew-symmetric matrix represented as Equation (1.13) [11].

$$Q(\omega) = \begin{bmatrix} 0 & \omega_3 & -\omega_2 & \omega_1 \\ -\omega_3 & 0 & \omega_1 & \omega_2 \\ \omega_2 & -\omega_1 & 0 & \omega_3 \\ -\omega_1 & -\omega_2 & -\omega_3 & 0 \end{bmatrix} \tag{1.13}$$

In order to minimize the electrical energy expended throughout the maneuver and have the cost actually represent the attitude control system's demand on the electrical power system, the electrical energy consumption must be characterized. To derive this electrical energy consumption relation, an equation describing the electrical power draw for a DC, steady state motor was derived in [3, 11, 12, 13] producing Equation (1.14).

$$P(t) = \frac{R}{K_T^2} (\tau_i(t) + \beta \, \Omega_i(t))^2 + \tau_i(t) \Omega_i(t) + \beta \, \Omega_i(t)^2 \tag{1.14}$$

where P is the electrical power drawn at a particular time, t, from a particular reaction wheel rotating at an angular rate, Ω_i, with an applied torque, τ_i, while R is the reaction wheel's armature resistance, K_T is the torque constant, and β is the coefficient of viscous friction. Together, the first term in Equation (1.14) accounts for the copper losses in the reaction wheel system, the second term represents the mechanical power, while the third term represents the friction losses [3, 11, 12, 13]. Over the duration of a maneuver, "each reaction wheel motor may alternate between being a load $[P_i(t) > 0]$ or acting as a source $[P_i(t) < 0]$" [3]. However, attitude control systems are not regenerative systems. Therefore, the power produced when the reaction wheels act as sources is dissipated through a ballast resistor [3]. As a result, Equation (1.14) is rewritten so that if the calculated power for a particular reaction wheel in a single instant is negative, it is set to zero. Equation (1.15) displays this relation mathematically.

$$P^+(t) = \begin{cases} P(t) & \text{if } P(t) > 0 \\ 0 & \text{if } P(t) \leq 0 \end{cases} \tag{1.15}$$

In order to calculate the electrical energy consumption over the duration of the maneuver for such a non-regenerative system, Equation (1.15) is integrated over the slew time as shown in Equation (1.16).

$$\varepsilon^+ = \int_{t_0}^{t_f} P^+(t)dt \tag{1.16}$$

Due to the nonsmooth nature of Equation (1.15) though, Equation (1.16) is challenging to use as is for defining a cost functional in an optimal control problem [2, 3]. Reference [2] goes on to solve for Equation (1.16) as a cost functional proving it is possible to use, however, completing this work is outside the scope of this thesis. Alternatively, Equation (1.14) will be used as a proxy cost functional in this thesis and the resulting power draw profile for each maneuver will be integrated in order to estimate Equation (1.16) to evaluate the maneuver's total electrical energy consumption.

B.   SPACECRAFT MODEL PARAMETERS

For this research, the Lunar Reconnaissance Orbiter (LRO) was chosen as the spacecraft representation. The National Aeronautics and Space Administration (NASA) launched the LRO on June 18, 2009 on the Exploration Mission to photograph the lunar surface [14]. The LRO began the Exploration Mission within days of inserting into lunar orbit and completed the mission by September 2010; with its main mission completed and all systems working, LRO's purpose on orbit was immediately expanded to both exploration and science using its array of seven unique sensor payloads designed to collect data on the lunar surface [14, 15]. After spending an additional two years in its initial low polar orbit around the Moon, the LRO transferred into a stable, elliptical orbit with perigee near the southern pole [15]. Now, 10 years after launch, the LRO is still operational in orbit around the Moon and executing assigned missions. The LRO has collected and transmitted an incredible amount of data allowing scientists to explore and study the lunar surface like never before. As long as the LRO is operational, it will be tasked to complete exploration

and scientific missions in order to further mankind's understanding of Earth's precious Moon.

Figure 1.   Artist's Rendition of the LRO in Orbit around the Moon.
Source: [16].

To support these wide variety of missions, the LRO has seven scientific payload systems on board [17]. To protect these payload systems, the LRO has attitude restrictions limiting where the instruments can point and how fast the LRO can slew [1, 18]. Additionally, like any spacecraft's electrical power system, the LRO's electrical power system is required to power the payload systems and the entire supporting bus, including the attitude control system. Since the bus is required to function in between missions, the LRO restricts the payload system's power consumption by limiting the duration of data collection windows, effectively reducing the amount of collected scientific data. It would be possible to increase the allowable data collection window by creating new attitude control maneuvers that, a) point the spacecraft and its sensors quickly to the desired attitude and, b) minimize the attitude control system's power consumption. This kind of attitude maneuver would allow the payload systems to be in the correct position for a longer period of time and, thus, reallocates more power to the payload systems. Minimum energy and

reduced time attitude maneuvers would allow the LRO to gather more scientific data during its lifespan, optimizing its use while on orbit. In order to demonstrate the electrical energy consumption and time savings of such optimally designed attitude slews, two arbitrary desired attitude positions are chosen in order to find and compare an industry standard trajectory to multiple optimally designed trajectories.

An estimate of the LRO's inertia tensor in the spacecraft body frame, J, is a critical constant for this problem and is listed in Equation (1.17). The LRO body is restricted to not rotate faster than $|\omega_i(t)| \leq 0.13 \, ^\circ\!/_s$ when executing an attitude slew in order to minimize gyroscopic disturbance torques; this constraint is recorded in Equation (1.18). The LRO's attitude control system consists of four reaction wheels in a configuration pictured in Figure 2. The reaction wheel alignment matrix, Z, is listed in Equation (1.19). The alignment matrix resolves the components of each wheel's angular momentum into the spacecraft body frame. A single LRO reaction wheel has an inertia, J_w, listed in Equation (1.20). All reaction wheels are assumed to have the same inertia, J_w.
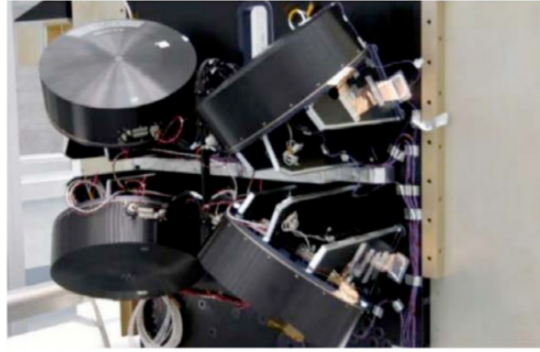
Figure 2.   LRO's Reaction Wheel Assembly. Source: [1].

$$J = \begin{bmatrix} 955.2 & 0 & 0 \\ 0 & 1687.4 & 0 \\ 0 & 0 & 1609.5 \end{bmatrix} kg \cdot m^2 \tag{1.17}$$

$$|\omega_i(t)| \leq 0.13 \, ^\circ\!/_s \tag{1.18}$$

$$Z = \begin{bmatrix} 0.81915 & 0.81915 & -0.81915 & -0.81915 \\ 0.40558 & -0.40558 & 0.40558 & -0.40558 \\ 0.40558 & 0.40558 & 0.40558 & 0.40558 \end{bmatrix} \qquad (1.19)$$

$$J_w = 0.231 kg \cdot m^2 \qquad (1.20)$$

No data is available for the LRO reaction wheel system's armature resistance, torque constant, or coefficient of viscous friction, three critical constants necessary to calculate the attitude control system's power draw. As a solution, the terminal resistance and torque constant of the reaction wheels present on the Naval Postgraduate School's Control & Optimization Laboratory's attitude control system testbed were used instead as the values are similar to a typical reaction wheel drive. The testbed consists of four Maxon Motors [19] with a terminal resistance as listed in Equation (1.21) and a torque constant represented with Equation (1.22). The Maxon Motor data sheet [19] did not provide the armature resistance, therefore the terminal resistance value was taken instead. The Maxon Motor data sheet also did not provide the motor's coefficient of viscous friction; as a substitute, the value in Equation (1.23) was estimated from reviewing available literature [20].

$$R = 0.343\Omega \qquad (1.21)$$

$$K_T = 0.0705 \, Nm/A \qquad (1.22)$$

$$\beta = 2.15e^{-5} \, Nm/rad/s \qquad (1.23)$$

C.   MANEUVER BOUNDARY CONDITIONS

Initial and final attitudes were chosen to define the desired orientations analyzed within this research and represented with quaternions, q, as was stated earlier. Furthermore, the maneuver was chosen to be "rest-to-rest" implying that the spacecraft will be stationary at the beginning and end of the maneuver; thus $\omega(t_0) = \omega(t_f) = [0,0,0]^T$. In order for the spacecraft to be at rest at the initial and final orientations, the reaction wheels must have the same initial and final rotation rates. This is demanded by the conservation of angular momentum when it is assumed there are no external torques applied to the system [18].

Although reaction wheels are typically set with bias in real spacecraft systems, for the analysis here, the reaction wheels will be assumed to be at rest at the initial and final time; thus $\mathbf{\Omega}(t_0) = \mathbf{\Omega}(t_f) = [0,0,0,0]^T$. The problem's boundary conditions are recorded in Equation (1.24).

$$\begin{aligned}
\boldsymbol{q}(t_o) &= [0,0,0,1]^T \\
\boldsymbol{q}(t_f) &= [-0.8026, 0.1498, -0.2264, 0.5312]^T \\
\boldsymbol{\omega}(t_o) &= \boldsymbol{\omega}(t_f) = [0,0,0]^T \, {}^{\circ}\!\!\Big/\!{}_S \\
\mathbf{\Omega}(t_o) &= \mathbf{\Omega}(t_f) = [0,0,0,0]^T \, rpm
\end{aligned} \tag{1.24}$$

With the dynamical model defined, the spacecraft platform characterized, the reaction wheel model detailed, and the boundary conditions of the maneuver identified, the industry standard Eigenaxis maneuver can be identified and optimally designed attitude trajectories can be generated as a result of solving optimal control problem formulations populated with these practical model constants presented in this section. The Eigenaxis maneuver solution will be found first, in the next chapter. This will provide the baseline maneuver duration and electrical energy consumption used to bracket the two optimally designed maneuvers later.

III. CONVENTIONAL EIGENAXIS MANEUVERING

Eigenaxis maneuvers are commonly used to conduct spacecraft slew maneuvers on orbit but are typically not the most time [21] or energy efficient [3] maneuver solutions. To demonstrate the characteristics of the Eigenaxis maneuver, the time and electrical energy cost will be evaluated in this chapter for the maneuver defined in Chapter II.

An Eigenaxis maneuver is a minimum distance solution to reorient a spacecraft from an initial to a final attitude. This maneuver is accomplished by rotating about a single axis defined by the required maneuver endpoints [8]. Because the rotation takes place around a single axis, the spacecraft can accelerate at its maximum angular acceleration until it reaches its body rotation rate limit. The spacecraft can continue rotating at this speed until it is time to decelerate in order to come to a rest at the end of the maneuver.

Assuming the initial quaternion is $\boldsymbol{q}(t_0) = [0,0,0,1]^T$, the Eigen axis, $\hat{\boldsymbol{e}}$, and angle of rotation, Φ, needed to conduct an Eigenaxis slew to a desired quaternion can be found from Equations (1.25) and (1.26) [8].

$$\Phi = 2\cos^{-1} q_4 \tag{1.25}$$

$$\hat{\boldsymbol{e}} = \begin{bmatrix} \dfrac{q_1}{\sin(\Phi/2)} \\ \dfrac{q_2}{\sin(\Phi/2)} \\ \dfrac{q_3}{\sin(\Phi/2)} \end{bmatrix} \tag{1.26}$$

Using Equation (1.25) and the final attitude quaternion $\boldsymbol{q}(t_f) = [-0.8026, 0.1498, -0.2264, 0.5312]^T$, the rotation angle about the Eigen axis, $\hat{\boldsymbol{e}}$, was found to be $\Phi = 115.8°$. Using Equation (1.26), the Eigen axis was calculated to be $\hat{\boldsymbol{e}} = [-0.9473, 0.1768, -0.2672]^T$.

Given the Eigenaxis and rotation angle along with a given spacecraft's body rotation rate limit and maximum angular acceleration, which was given as $|\alpha(t)| \leq 0.068\,°\!/\!_{s^2}$

, the critical time to reach the maximum rotation rate can be calculated along with the coast time (where the rate is constant at its maximum value) and total duration of the slew maneuver. Equations (1.27) through (1.29) were used to find these values [22].

$$t_{crit} = \frac{\omega_{max}}{\alpha_{max}} \tag{1.27}$$

$$t_{coast} = \frac{\Phi - \omega_{max} t_{crit}}{\omega_{max}} \tag{1.28}$$

$$t_{slew} = \frac{\Phi}{\omega_{max}} + \frac{\omega_{max}}{\alpha_{max}} \tag{1.29}$$

The critical time, coast time, and maneuver duration (slew time) define an acceleration profile that accomplish the maneuver about the Eigenaxis. The spacecraft will accelerate at it maximum acceleration until the critical time, $t_{crit} = 19.12s$, where it will begin its coast at the maximum allowable rate. The spacecraft will rotate at constant speed until $t_{crit} + t_{coast} = 891.0s$ when the spacecraft will initiate a deceleration in order to return to rest. The corresponding acceleration profile for the maneuver is given in Figure 3.
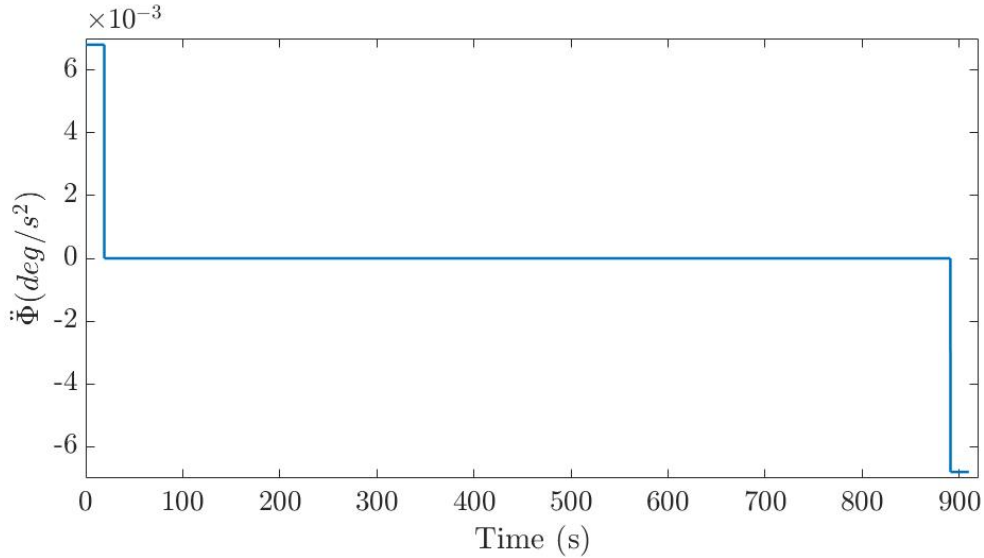
Figure 3.   Acceleration Profile for Eigenaxis Maneuver

14

The time integral of the acceleration profile can be taken to determine the maneuver velocity profile, shown in Figure 4. Figure 4 shows that the spacecraft does not exceed its maximum body rotation rate limit during the slew, maintaining its rotational speed at $|\omega_i(t)| \leq 0.13 \frac{\circ}{s}$ for the entire coast time. The body rotation rate starts and ends at zero for a rest-to-rest maneuver, as required by the problem definition's boundary conditions.
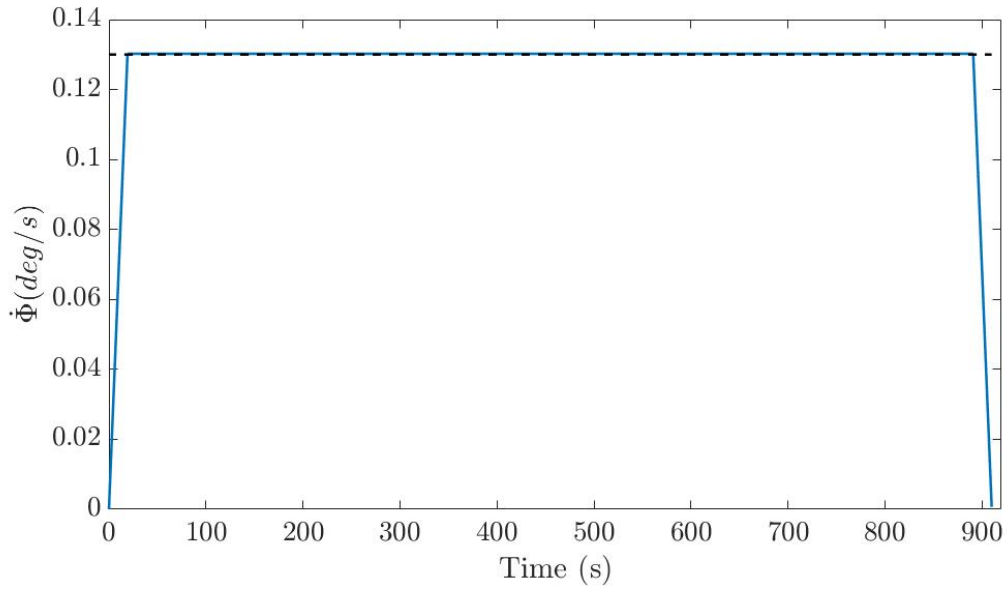
Figure 4.   Angular Velocity Profile for Eigenaxis Maneuver

Integrating the velocity profile from Figure 4 gives the position profile in Figure 5, which shows the rotation angle over the duration of this maneuver. Figure 5 shows that the spacecraft rotates $\Phi \approx 116°$ which is the required rotation angle calculated from Equation (1.25).
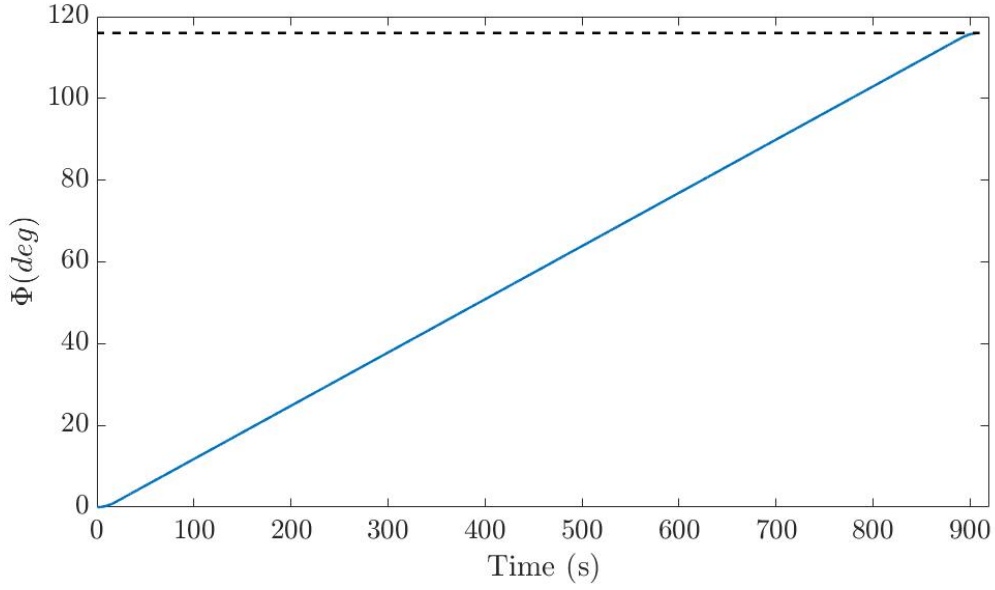
Figure 5.   Rotation Angle for Eigenaxis Maneuver

Given the Eigenaxis acceleration, rate, and position curves, the necessary reaction wheel torques and speeds can be solved in order to execute the slew using the reaction wheel actuators and also to calculate the Eigenaxis maneuver's electrical energy consumption.

The torque vector required on the spacecraft body at any instant is equal to the spacecraft's inertia matrix multiplied by the angular acceleration vector as denoted in Equation (1.30) [23].

$$^{B}\boldsymbol{\tau}_{s/c} = \boldsymbol{J}\,^{B}\boldsymbol{\alpha} \tag{1.30}$$

Since the spacecraft's angular acceleration in the body frame is equal to the spacecraft's acceleration around the Eigen axis, Equation (1.30) can be rewritten as Equation (1.31).

$$^{B}\boldsymbol{\tau}_{s/c} = \boldsymbol{J}\ddot{\Phi}\hat{\boldsymbol{e}} \tag{1.31}$$

In order to calculate the power required for this Eigenaxis maneuver, the torque for individual the reaction wheels must be derived from the spacecraft body torques. The torque in the body frame due to the wheels can be determined by mapping the wheel spin

16

axes to the body frame. This is done using the alignment matrix, Z, multiplied with the torque on the reaction wheels as written in Equation (1.32).

$$^{B}\boldsymbol{\tau}_{s/c} = \boldsymbol{Z}\boldsymbol{\tau}_{w} \tag{1.32}$$

To find the reaction wheel torques, Equation (1.32) is multiplied on each side by the pseudoinverse of Z. The pseudoinverse is used because the reaction wheel alignment matrix for a redundant reaction wheel attitude control system is non-square. The pseudoinverse is calculated as Equation (1.33) [8].

$$\boldsymbol{Z}^{\dagger} = (\boldsymbol{Z}^{T}\boldsymbol{Z})^{-1}\boldsymbol{Z}^{T} \tag{1.33}$$

Given the reaction wheel alignment matrix, the spacecraft inertia tensor, the Eigenaxis acceleration and the Eigenaxis, Equations (1.31) and (1.32) can be rearranged and combined to form Equation (1.34) which gives the reaction wheel torque vector.

$$\boldsymbol{\tau}_{w} = \boldsymbol{Z}^{\dagger}\boldsymbol{J}\ddot{\Phi}\hat{\boldsymbol{e}} \tag{1.34}$$

Using the Eigenaxis acceleration profile from Figure 3 in Equation (1.34) gives the reaction wheel torque profiles for all four reaction wheels as plotted in Figure 6. Initial torques are applied by all four reaction wheels until the body rotation rate limit is reached at $t_{crit} = 19.12s$. All reaction wheel torques are then zeroed for the duration of the coast period until $t_{crit} + t_{coast} = 891.0s$. To bring the spacecraft to rest at the final attitude, the reaction wheel torques are applied in a negative sense to induce a braking torque.
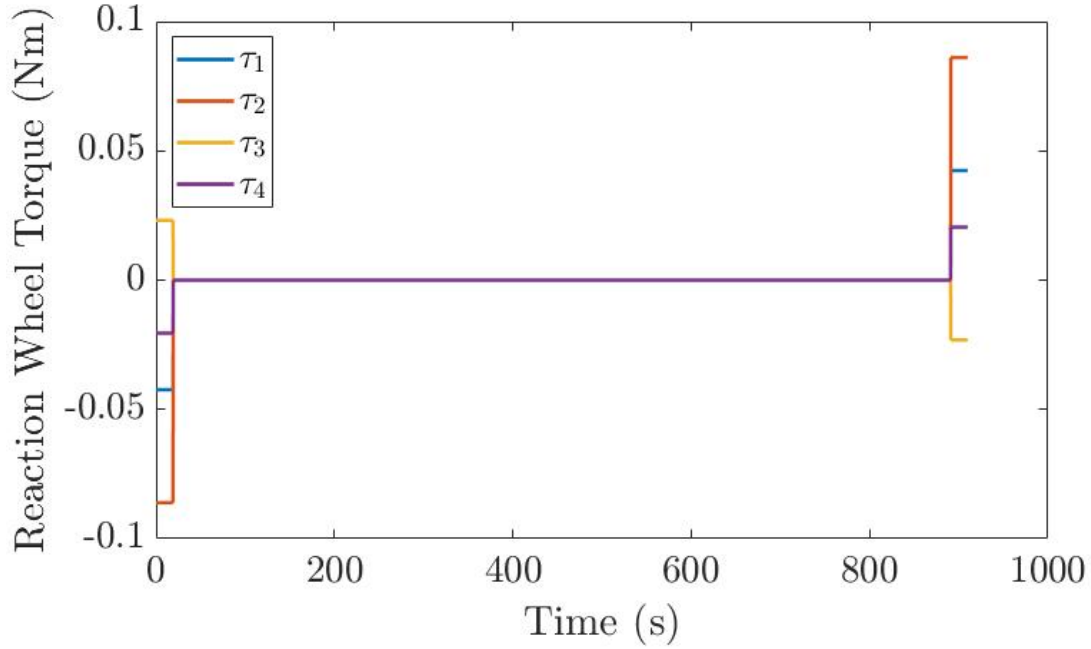
Figure 6.   Reaction Wheel Control Torques for Eigenaxis Maneuver

With the reaction wheel control torques determined, the reaction wheel rotation rates need to be calculated in order to find the electrical energy consumption of the Eigenaxis maneuver. To find the reaction wheel rotation rates, the conservation of angular momentum for the spacecraft system is considered as in Equation (1.35).

$$^{B}\boldsymbol{H}_{s/c} + {}^{B}\boldsymbol{H}_{w} = 0 \tag{1.35}$$

where $^{B}\boldsymbol{H}_{s/c}$ is the angular momentum of the spacecraft in the body frame and $^{B}\boldsymbol{H}_{w}$ is the angular momentum of the reaction wheels in the body frame. The angular momentum of the spacecraft in the body frame can be rewritten as a function of the spacecraft's inertia, the Eigenaxis rotation rate, and the Eigenaxis in Equation (1.36).

$$^{B}\boldsymbol{H}_{s/c} = \boldsymbol{J}\dot{\Phi}\hat{\boldsymbol{e}} \tag{1.36}$$

Similarly, $^{B}\boldsymbol{H}_{w}$ can be rewritten as a function of the reaction wheel alignment matrix, the reaction wheel's inertia, and the reaction wheel rotation rates as Equation (1.37).

18

$$^{B}\boldsymbol{H}_{w} = \boldsymbol{Z}J_{w}\boldsymbol{\Omega} \tag{1.37}$$

Substituting Equations (1.36) and (1.37) into Equation (1.35) and rearranging gives Equation (1.38) which yields the reaction wheel rotation rate vector.

$$\boldsymbol{\Omega} = -\boldsymbol{Z}^{\dagger}J_{w}^{-1}\boldsymbol{J}\dot{\Phi}\hat{\boldsymbol{e}} \tag{1.38}$$

The reaction wheel rotation rates are plotted for the Eigenaxis maneuver in Figure 7. Each reaction wheel accelerates according to its applied torque from Figure 6 until the maximum body rotation rate is reached. The reaction wheel rates then stay constant during the coast and are reduced back to zero to bring the spacecraft to rest. The final reaction wheel rotation rates match the required boundary conditions, confirming that the spacecraft body has returned to rest as well.
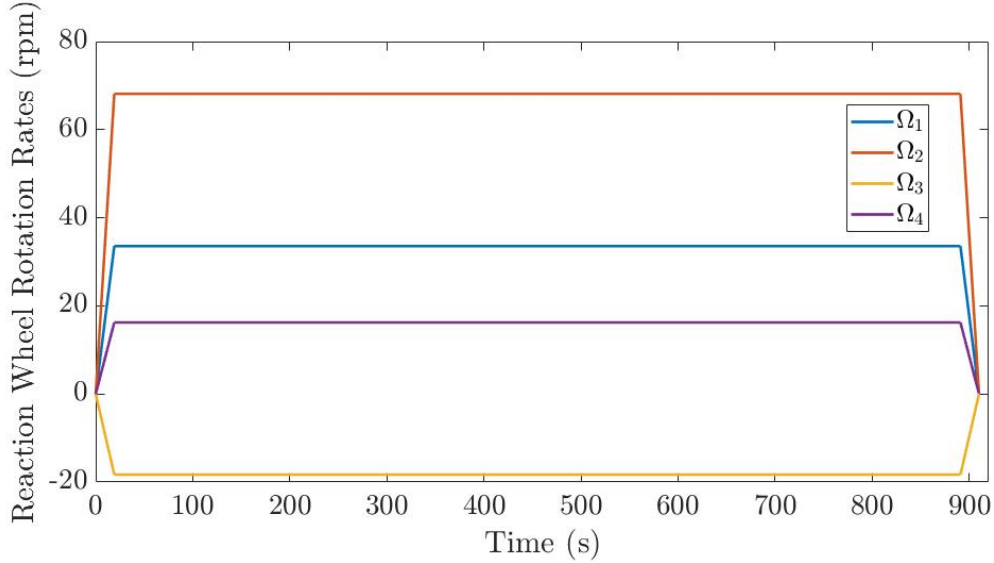
Figure 7.   Reaction Wheel Rotation Rates for Eigenaxis Maneuver

Using the reaction wheel rates and torque profile, the total power needed to perform this Eigenaxis maneuver can be calculated using Equation (1.14). Figure 8 plots the power draw for each reaction wheel.
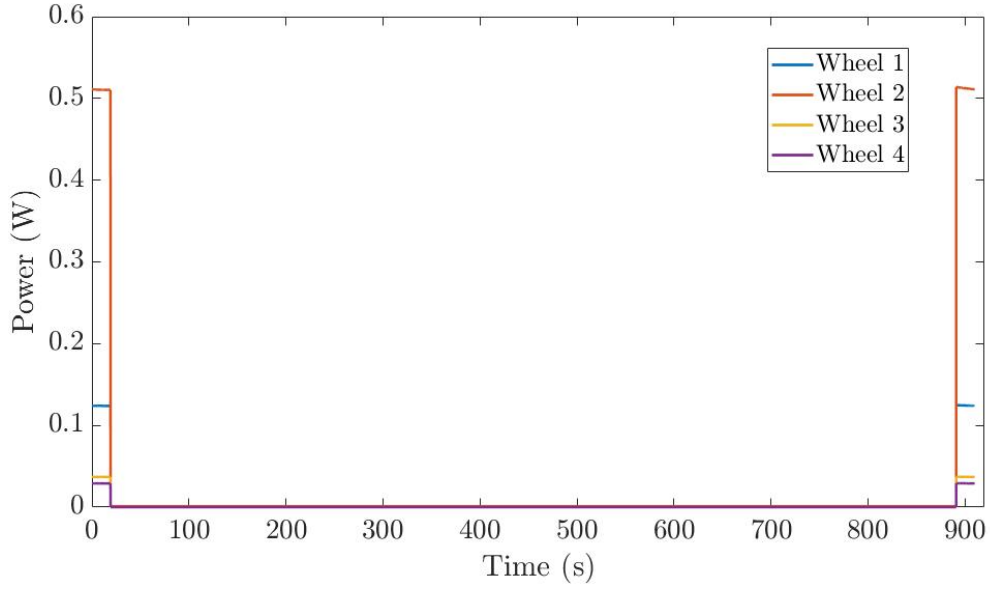
Figure 8.   Eigenaxis Maneuver Power Draw

The individual reaction wheel power curves are integrated and then summed to plot the cumulative consumed electrical energy for operating all four reaction wheels in Figure 9. Performing the Eigenaxis maneuver requires $E = 28.12J$ of electrical energy to successfully execute the attitude slew within $t_{slew} = 910.1s$.

20
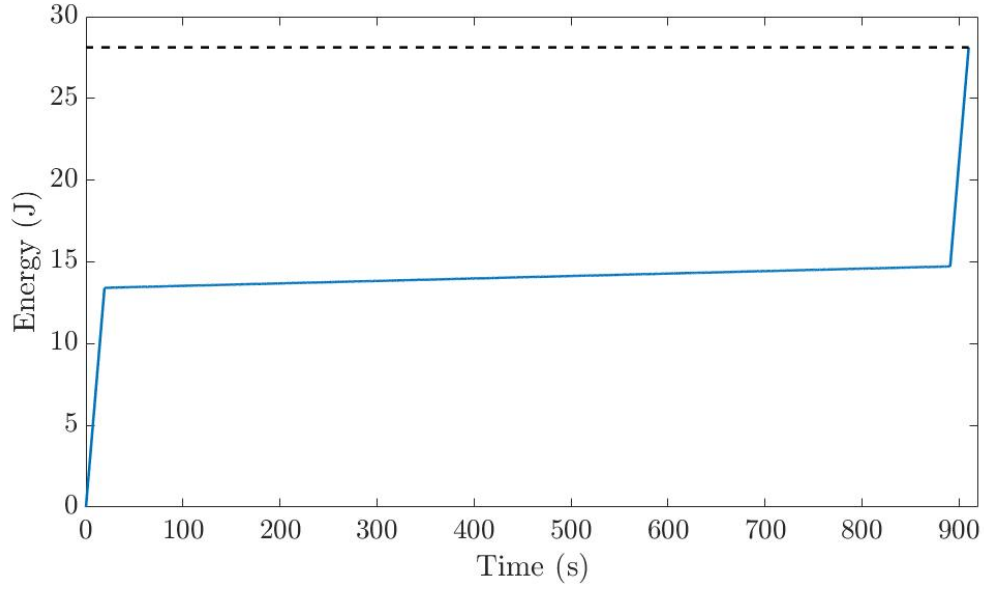
Figure 9.   Eigenaxis Maneuver Total Electrical Energy Consumption

Although the Eigenaxis maneuver is the industry standard, an optimally designed maneuver can reduce either time, electrical energy consumption, or a combination of both [3, 11]. With the standard Eigenaxis maneuver costs determined in this chapter, this thesis will now characterize two new maneuvers: a Minimum Electrical Energy, Fixed-Time (MEEFT) maneuver and an Equivalent Electrical Energy, Reduced Time (EEERT) maneuver. Figure 10 illustrates the conceptual relationship identified in [3] between the costs of all three maneuvers discussed within this thesis. The MEEFT maneuver will take as much time to complete the same maneuver as the Eigenaxis slew but is expected to consume less electrical energy. The EEERT maneuver will consume the same amount of electrical energy but is expected to take less time. The next two chapters apply optimal control theory in order to find the MEEFT and the EEERT maneuvers and characterize their electrical energy costs. The dotted line in Figure 10 represents additional maneuvers that will be found that cost less time and electrical energy; this maneuver data set forms the trade space on time and electrical energy for this particular set of maneuver endpoints.

21
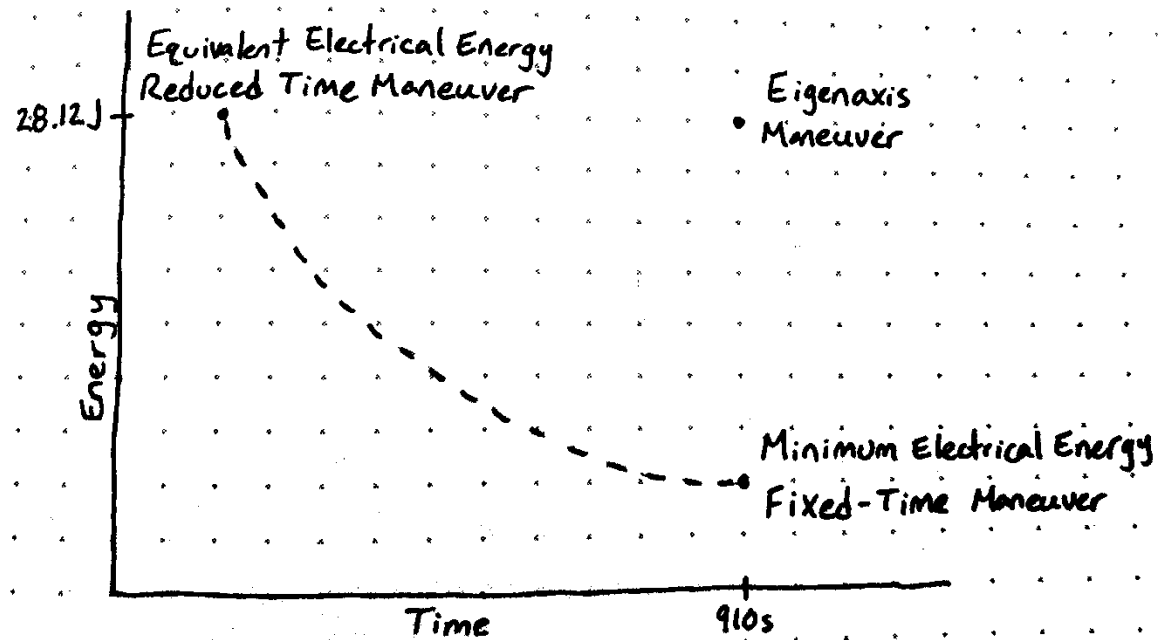
Figure 10.   Conceptual Operating Envelope for Maneuver Time and
Electrical Energy. Adapted from [3].

IV.   MINIMUM ELECTRICAL ENERGY, FIXED-TIME (MEEFT) MANEUVER

Optimal control theory is applied in this chapter in order to find a maneuver that consumes less electrical energy while completing the maneuver in the same amount of time as the standard Eigenaxis slew; this maneuver is referred to as the Minimum Electrical Energy, Fixed-Time (MEEFT) maneuver and is highlighted in Figure 11.
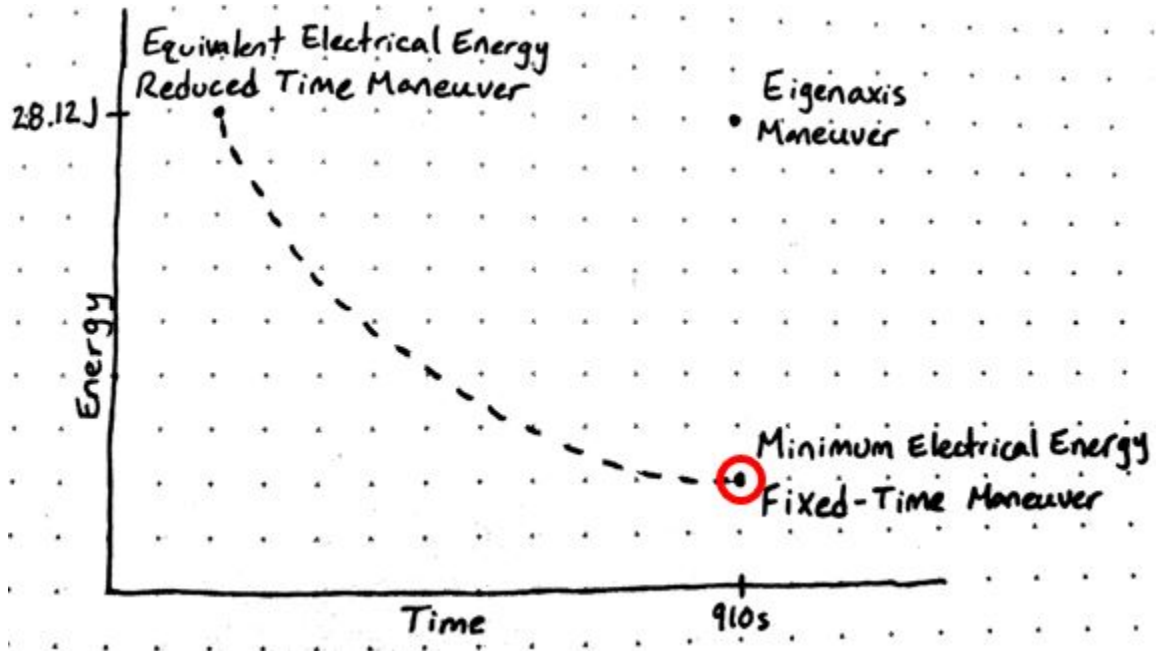
Figure 11.   Conceptual Cost Relation Between Minimum Electrical
Energy, Fixed-Time Maneuver and Eigenaxis Maneuver

In order to find this minimum electrical energy solution, the problem must be properly formulated. The necessary conditions for optimality must also be determined to evaluate the solution. When the problem formulation is built and the necessary conditions identified, the problem will be solved numerically using DIDO [24]. DIDO is a MATLAB tool box for solving optimal control problems. This chapter will present the resulting MEEFT maneuver solution.

23

A.   MEEFT PROBLEM FORMULATION

To build the MEEFT problem formulation for optimal control, the four components of an attitude quaternion, the three spacecraft body rotation rates, and the four reaction wheel rotation rates were set as the state variables. The spacecraft's attitude is controlled via torque applied to the four reaction wheels. Thus, these four torques were set as the control variables.

To find the minimum electrical energy maneuver, the running cost function is set equal to a summation of each reaction wheel's individual power consumption defined by Equation (1.14). Since only electrical energy is being minimized and is already accounted for in the running cost, the endpoint cost is zero. The cost functional is then written as Equation (1.39).

$$J(\boldsymbol{x}(\cdot),\boldsymbol{u}(\cdot),t) = \sum_{i=1}^{4} \int_{t_0}^{t_f} \frac{R}{K_T^2}(\tau_i + \beta\,\Omega_i)^2 + \tau_i\Omega_i + \beta\,\Omega_i^2\,dt \tag{1.39}$$

The non-linear dynamical model of the spacecraft defined in Chapter II is used to define the system dynamics. The boundary conditions stated in Equation (1.24) are used along with the spacecraft and reaction wheel constants outlined in Equations (1.17), (1.19), and (1.20). Additionally, the spacecraft body rotation rate constraint from Equation (1.18) is included as a path constraint in the problem formulation to prevent the spacecraft from exceeding the specified rate limit. Gathering these equations allows the problem formulation to be constructed in the standard form [4], as shown in Figure 12.

24

$$
P_{MEEFT}
\begin{cases}
\text{States:} & x = \begin{bmatrix} q \\ \omega \\ \Omega \end{bmatrix} \in \mathbb{R}^{4+3+4} \\[2ex]
\text{Control:} & u = [\tau] \in \mathbb{R}^4 \\[2ex]
\text{Minimize:} & J(x(\cdot), u(\cdot), t) = \int_{t_o}^{t_f} \sum_{i=1}^{4} \frac{R}{K_T^2}(\tau_i(t) + \beta\Omega_i(t))^2 + \tau_i(t)\Omega_i(t) + \beta\Omega_i(t)^2 \, dt \\[2ex]
\text{Subject to:} & \\
& \dot{x} = \begin{bmatrix} \frac{1}{2}Q(\omega)q \\ J^{-1}(-\omega \times (J\omega + ZJ_w\Omega) - Z\tau) \\ \frac{\tau}{J_w} \end{bmatrix} \\[4ex]
& t_o = 0; \; x(t_o) = \begin{bmatrix} [0,0,0,1]^T \\ [0,0,0]^T \\ [0,0,0,0]^T \end{bmatrix} \\[3ex]
& t_f = 910; \; x(t_f) = \begin{bmatrix} [-0.8026, 0.1498, -0.2264, 0.5312]^T \\ [0,0,0]^T \\ [0,0,0,0]^T \end{bmatrix} \\[3ex]
& |\omega_i(t)| < 0.13°/s
\end{cases}
$$

Constants:

$$
J = \begin{bmatrix} 955.2 & 0 & 0 \\ 0 & 1687.4 & 0 \\ 0 & 0 & 1609.5 \end{bmatrix} (kg \cdot m^2) \qquad\qquad R = 0.343 \, \Omega
$$

$$
J_w = 0.231 \, kg \cdot m^2 \qquad\qquad\qquad K_T = 70.5 * 10^{-3} \, Nm/A
$$

$$
Z = \begin{bmatrix} 0.81915 & 0.81915 & -0.81915 & -0.81915 \\ 0.40558 & -0.40558 & 0.40558 & -0.40558 \\ 0.40558 & 0.40558 & 0.40558 & 0.40558 \end{bmatrix} \qquad \beta = 2.15 * 10^{-5} \frac{Nm}{rad/s}
$$

Figure 12.   Minimum Electrical Energy, Fixed-Time Problem
Formulation

B.   NECESSARY CONDITIONS FOR OPTIMALITY

A numerical solution to P_{MEEFT} must meet the necessary conditions for optimality which are obtained through an application of Pontryagin's Principle. To find the necessary conditions, the Hamiltonian or Lagrangian of the Hamiltonian is built first. Then, the necessary conditions are found using the Adjoint equations, the Stationary Conditions, the Complementarity Conditions, the Hamiltonian Value Condition, the Hamiltonian Evolution Equation, and the Transversality conditions [4].

The Hamiltonian consists of the running cost, F, added to the costates, λ, dotted together with the time derivative of each state, $f = \dot{x}$ [4]. Equation (1.40) mathematically represents this relationship.

$$H = F + \boldsymbol{\lambda}^T \boldsymbol{f} \tag{1.40}$$

If path constraints are included in the problem statement, which they are for the reorientation problem of this thesis, the Lagrangian of the Hamiltonian must be used instead. The Lagrangian of the Hamiltonian is the Hamiltonian from Equation (1.40) summed with the path covectors, $\boldsymbol{\mu}$, dotted together with the path constraint equations, $\boldsymbol{h}$ [4]. The Lagrangian of the Hamiltonian is written as Equation (1.41).

$$\bar{H} = H + \boldsymbol{\mu}^T \boldsymbol{h} \tag{1.41}$$

For the chosen maneuver, the Hamiltonian is written according to Equation (1.40), producing Equation (1.42).

$$
\begin{aligned}
H = & \frac{R}{K_T{}^2}(\tau_1{}^2 + 2\beta\tau_1\Omega_1 + \beta^2\Omega_1{}^2) + \tau_1\Omega_1 + \beta\,\Omega_1{}^2 \\
& + \frac{R}{K_T{}^2}(\tau_2{}^2 + 2\beta\tau_2\Omega_2 + \beta^2\Omega_2{}^2) + \tau_2\Omega_2 + \beta\,\Omega_2{}^2 \\
& + \frac{R}{K_T{}^2}(\tau_3{}^2 + 2\beta\tau_3\Omega_3 + \beta^2\Omega_3{}^2) + \tau_3\Omega_3 + \beta\,\Omega_3{}^2 \\
& + \frac{R}{K_T{}^2}(\tau_4{}^2 + 2\beta\tau_4\Omega_4 + \beta^2\Omega_4{}^2) + \tau_4\Omega_4 + \beta\,\Omega_4{}^2 \\
& + 0.5\lambda_{q_1}(\omega_3 q_2 - \omega_2 q_3 + \omega_1 q_4) + 0.5\lambda_{q_2}(-\omega_3 q_1 + \omega_1 q_3 + \omega_2 q_4) \\
& + 0.5\lambda_{q_3}(\omega_2 q_1 - \omega_1 q_2 + \omega_3 q_4) + 0.5\lambda_{q_4}(-\omega_1 q_1 - \omega_2 q_2 + \omega_3 q_3) \\
& + \lambda_{\omega_1}(J_1^{-1}(-\omega_2(J_3\omega_3 + J_w(Z_{31}\Omega_1 + Z_{32}\Omega_2 + Z_{33}\Omega_3 + Z_{34}\Omega_4)) \\
& + \omega_3(J_2\omega_2 + J_w(Z_{21}\Omega_1 + Z_{22}\Omega_2 + Z_{23}\Omega_3 + Z_{24}\Omega_4)) \\
& - Z_{11}\tau_1 - Z_{12}\tau_2 - Z_{13}\tau_3 - Z_{14}\tau_4) \\
& + \lambda_{\omega_2}(J_2^{-1}(-\omega_1(J_3\omega_3 + J_w(Z_{31}\Omega_1 + Z_{32}\Omega_2 + Z_{33}\Omega_3 + Z_{34}\Omega_4)) \\
& + \omega_3(J_1\omega_1 + J_w(Z_{11}\Omega_1 + Z_{12}\Omega_2 + Z_{13}\Omega_3 + Z_{14}\Omega_4)) \\
& - Z_{21}\tau_1 - Z_{22}\tau_2 - Z_{23}\tau_3 - Z_{24}\tau_4) \\
& + \lambda_{\omega_3}(J_3^{-1}(-\omega_1(J_2\omega_2 + J_w(Z_{21}\Omega_1 + Z_{22}\Omega_2 + Z_{23}\Omega_3 + Z_{24}\Omega_4)) \\
& + \omega_2(J_1\omega_1 + J_w(Z_{11}\Omega_1 + Z_{12}\Omega_2 + Z_{13}\Omega_3 + Z_{14}\Omega_4)) \\
& - Z_{31}\tau_1 - Z_{32}\tau_2 - Z_{33}\tau_3 - Z_{34}\tau_4) \\
& + \lambda_{\Omega_1}\frac{\tau_1}{J_w} + \lambda_{\Omega_2}\frac{\tau_2}{J_w} + \lambda_{\Omega_3}\frac{\tau_3}{J_w} + \lambda_{\Omega_4}\frac{\tau_4}{J_w}
\end{aligned}
\tag{1.42}
$$

The Lagrangian of the Hamiltonian is then written as Equation (1.43).

$$\bar{H} = H + \mu_1\omega_1 + \mu_2\omega_2 + \mu_3\omega_3 \tag{1.43}$$

The Adjoint equations introduce the concept of a costate and define the dynamics of each costate in relation to the problem statement [4]. A costate is the dual of each state defined in the problem statement. These duals provide a way to measure the state vector. The costates are annotated as λ_{x_i} where x represents a state and i represents the number of the state, e.g. λ_{q_1} for q_1 or λ_{ω_3} for ω_3. The Adjoint equations define the dynamics between the negative time derivative of the costate and the partial derivative of the Lagrangian of the Hamiltonian with respect to the related state [4]. The Adjoint equations can be written as Equation (1.44).

$$\frac{\partial \bar{H}}{\partial x_i} = -\dot{\lambda}_{x_i} \tag{1.44}$$

Equation (1.44) produced a set of 11 equations describing the behavior of the rate of change of the costates. Although these equations describe the trajectory of the costates throughout the solution, they are not easy to use in the validation and verification process due to their complexity. To illustrate this, three of the Adjoint equations associated to the problem P$_{\text{MEEFT}}$ are written as Equations (1.45) through (1.47).

$$\dot{\lambda}_{q_1} = -0.5(-\omega_3\lambda_{q_2} + \omega_2\lambda_{q_3} - \omega_1\lambda_{q_4}) \tag{1.45}$$

$$-\dot{\lambda}_{\omega_1} = 0.5(q_4\lambda_{q_1} + q_3\lambda_{q_2} - q_2\lambda_{q_3} - q_1\lambda_{q_4})$$
$$+ \frac{\lambda_{\omega_2}}{J_2}(-J_3\omega_3 - J_w(Z_{31}\Omega_1 + Z_{32}\Omega_2 + Z_{33}\Omega_3 + Z_{34}\Omega_4) + J_1\omega_3) \tag{1.46}$$
$$+ \frac{\lambda_{\omega_3}}{J_3}(-J_2\omega_2 - J_w(Z_{21}\Omega_1 + Z_{22}\Omega_2 + Z_{23}\Omega_3 + Z_{24}\Omega_4) + J_1\omega_2) + \mu_{\omega_1}$$

$$-\dot{\lambda}_{\Omega_1} = \frac{2R}{K_T^2}\beta\tau_1 + \frac{2R}{K_T^2}\beta^2\Omega_1 + 2\beta\,\Omega_1 + \frac{\lambda_{\omega_1}}{J_1}(-\omega_2 J_w Z_{31} + \omega_3 J_w Z_{21})$$
$$+ \frac{\lambda_{\omega_2}}{J_2}(-\omega_1 J_w Z_{31} + \omega_3 J_w Z_{11}) + \frac{\lambda_{\omega_3}}{J_3}(-\omega_1 J_w Z_{21} + \omega_2 J_w Z_{11}) + \tau_1 \tag{1.47}$$

Pontryagin's Hamiltonian Minimization Condition includes two parts: the Stationary condition and the Complementarity condition. The Stationary condition aims to define the control values in terms of states and costates [4]. This is accomplished by setting the partial derivative of the Lagrangian of the Hamiltonian with respect to each of the single controls equal to zero and solving the resulting equation [4]. The Stationary condition is written mathematically as Equation (1.48).

$$\frac{\partial \bar{H}}{\partial u_i} = 0 \tag{1.48}$$

Using Equation (1.43) in Equation (1.48), produces the set of Equations (1.49) through (1.52). Although Equations (1.49) through (1.52) can be rearranged to describe the reaction wheel costates over the duration of the maneuver and are necessary conditions, due to their complexity, they will also not be used to check for optimality within this thesis.

$$\tau_1 = \frac{K_T^2}{2R}\left(\frac{\lambda_{\omega_1}Z_{11}}{J_1} + \frac{\lambda_{\omega_2}Z_{21}}{J_2} + \frac{\lambda_{\omega_3}Z_{31}}{J_3} - \frac{\lambda_{\Omega_1}}{J_w} - \Omega_1\right) - \beta\,\Omega_1 \tag{1.49}$$

$$\tau_2 = \frac{K_T^2}{2R}\left(\frac{\lambda_{\omega_1}Z_{12}}{J_1} + \frac{\lambda_{\omega_2}Z_{22}}{J_2} + \frac{\lambda_{\omega_3}Z_{32}}{J_3} - \frac{\lambda_{\Omega_2}}{J_w} - \Omega_2\right) - \beta\,\Omega_2 \tag{1.50}$$

$$\tau_3 = \frac{K_T^2}{2R}\left(\frac{\lambda_{\omega_1}Z_{13}}{J_1} + \frac{\lambda_{\omega_2}Z_{23}}{J_2} + \frac{\lambda_{\omega_3}Z_{33}}{J_3} - \frac{\lambda_{\Omega_3}}{J_w} - \Omega_3\right) - \beta\,\Omega_3 \tag{1.51}$$

$$\tau_4 = \frac{K_T^2}{2R}\left(\frac{\lambda_{\omega_1}Z_{14}}{J_1} + \frac{\lambda_{\omega_2}Z_{24}}{J_2} + \frac{\lambda_{\omega_3}Z_{34}}{J_3} - \frac{\lambda_{\Omega_4}}{J_w} - \Omega_4\right) - \beta\,\Omega_4 \tag{1.52}$$

The Complementarity Conditions characterize the behavior of the covectors as a function of the path constraints over the duration of the solution [4]. The Complementarity condition is generalized in the form written in Equation (1.53).

$$\mu := \begin{bmatrix} \geq 0 \text{ when } h = h_{\max} \\ = 0 \text{ when } h_{\min} < h < h_{\max} \\ \leq 0 \text{ when } h = h_{\min} \end{bmatrix} \tag{1.53}$$

Inserting the path constraints for problem P$_{\text{MEEFT}}$ into Equation (1.53) gives Equation (1.54). Since these conditions explicitly describe the behavior of the covectors, they are also necessary conditions for an optimal solution. Moreover, they are simple to verify.

$$\mu_i := \begin{bmatrix} \geq 0 \text{ when } \omega_i = 0.13 \\ = 0 \text{ when } -0.13 < \omega_i < 0.13 \\ \leq 0 \text{ when } \omega_i = -0.13 \end{bmatrix} \tag{1.54}$$

The Hamiltonian Value Condition determines the value of the Hamiltonian at the final time [4]. The final Hamiltonian value at the final time is equal to the negative partial derivative of the Endpoint Lagrangian with respect to the final time [4]. Mathematically, the Hamiltonian Value Condition is represented as Equation (1.55).

$$\bar{H}[@t_f] = -\frac{\partial \bar{E}}{\partial t_f} \tag{1.55}$$

To find the final value of the Hamiltonian according to Equation (1.55), the Endpoint Lagrangian must first be created. The Endpoint Lagrangian is equal to the Endpoint cost added to the end costates, ν, dotted together with e, the difference between each state and its endpoint boundary condition. The Endpoint Lagrangian is written as in Equation (1.56).

$$\bar{E} = E + \nu^T e \tag{1.56}$$

The Endpoint Lagrangian for this problem is found to be Equation (1.57).

$$\begin{aligned} \bar{E} = &\nu_{q_1}(q_1^f + 0.8026) + \nu_{q_2}(q_2^f - 0.1498) + \nu_{q_3}(q_3^f + 0.2264) \\ &+ \nu_{q_4}(q_4^f - 0.5312) + \nu_{\omega_1}\omega_1^f + \nu_{\omega_2}\omega_2^f + \nu_{\omega_3}\omega_3^f + \nu_{\Omega_1}\Omega_1^f + \nu_{\Omega_2}\Omega_2^f \\ &+ \nu_{\Omega_3}\Omega_3^f + \nu_{\Omega_4}\Omega_4^f + \nu_t(t_f - 910) \end{aligned} \tag{1.57}$$

Applying Equation (1.55) to Equation (1.57) produces Equation (1.58), which provides no useful information as it shows the final value of the Lagrangian of the Hamiltonian is equal to an unknown constant.

$$\bar{H}[@t_f] = -v_t = const \tag{1.58}$$

The Hamiltonian Evolution Equation, predicts how the lower Hamiltonian should vary with respect to time over the optimal control solution [4]. The Hamiltonian Evolution Equation is defined as the time derivative of the Lagrangian of the Hamiltonian equal to the partial derivative of the Lagrangian of the Hamiltonian with respect to time [4]. The Hamiltonian Evolution Equation is written as Equation (1.59) where $\bar{H}$ in the total derivative is interpreted as the lower Hamiltonian.

$$\frac{d\bar{H}}{dt} = \frac{\partial \bar{H}}{\partial t} \tag{1.59}$$

The Hamiltonian Evolution Equation defines Equation (1.60) for the problem formulation in Figure 12.

$$\frac{d\bar{H}}{dt} = \frac{\partial \bar{H}}{\partial t} = 0 \tag{1.60}$$

The problem P$_{MEEFT}$ is time invariant as shown by Equation (1.60), therefore, when combined with Equation (1.58), the lower Hamiltonian must be constant throughout an optimal solution with a value of v_t. Equation (1.60) is a critical necessary condition a solution must meet for optimality and is powerful within this thesis

Lastly, the Transversality conditions can be used to determine boundary conditions on the Adjoint variables [4]. These conditions are found by setting the final value of each costate equal to the partial derivative of the Endpoint Lagrangian with respect to the reciprocal state final condition [4]. The Transversality conditions can be found using Equation (1.61).

$$\lambda_{x_i}(t_f) = \frac{\partial \bar{E}}{\partial x_{i_f}} \tag{1.61}$$

When Equation (1.61) was applied to Equation (1.57), a set of 11 equations were produced; one example equation from each group of states is displayed in Equations (1.62) through (1.64).

$$\lambda_{q_1}(t_f) = \nu_{q_1} \tag{1.62}$$

$$\lambda_{\omega_1}(t_f) = \nu_{\omega_1} \tag{1.63}$$

$$\lambda_{\Omega_1}(t_f) = \nu_{\Omega_1} \tag{1.64}$$

As Equations (1.62) through (1.64) show, the Transversality conditions do not provide any additional information defining the Adjoint boundary conditions since the values of the end costates, ν, are all unknown. As a result, the Transversality conditions cannot be used to check for optimality for the P$_{\text{MEEFT}}$ solution. The remaining Transversality conditions along with the rest of the Adjoint equations are recorded in the Appendix for the interested reader.

To establish if a particular solution is optimal, the solution must be checked against the necessary conditions identified in this section. In this thesis, an optimal solution is vetted using the Complementarity Conditions from Equation (1.54), the Hamiltonian Value Condition from Equation (1.58), and the Hamiltonian Evolution Equation from Equation (1.60). To further confirm the validity of a solution, the optimal control should be propagated through the dynamics of the spacecraft in Equations (1.9), (1.10), and (1.12). The propagated solution should meet the boundary conditions defined in the problem formulation to be feasible.

C.   MEEFT NUMERICAL SOLUTION

With Pontryagin's Principle applied to analyze the MEEFT problem formulation and the necessary conditions identified, the problem was coded into DIDO to solve for a numerical solution.

Canonical and designer unit scaling [25] was applied to each state, control, path constraint, and cost in order to scale the search spaces and the dynamics, which is a best practice [4] for finding a numerical solution. Table 1 enumerates the scale factors used to

find a solution while Equations (1.65) through (1.72) explicitly state how each scaling factor was applied to the variables.

Table 1.   Scale Factors for Minimum Electrical Energy, Fixed-Time Maneuver

Canonical Scaling Units	
Value	Scale
C	0.0230
Designer Scaling Units	
Value	Scale
ε_q (1-4)	0.15
ε_ω (1-3)	0.004
ε_Ω (1-4)	15.2
ε_τ (1-4)	1
ε_t	10
ε_e (1-4)	0.001
ε_e (5-7)	0.001
ε_e (8-11)	1
ε_p (1-3)	0.01, 1, 1
ε_{cost}	0.1

$$q = \varepsilon_q \tilde{q} \tag{1.65}$$

$$\omega = C\varepsilon_\omega \tilde{\omega} \tag{1.66}$$

$$\Omega = C\varepsilon_\Omega \tilde{\Omega} \tag{1.67}$$

$$\tau = C^2 \varepsilon_\tau \tilde{\tau} \tag{1.68}$$

$$t = \varepsilon_t \tilde{t} \tag{1.69}$$

$$e = \varepsilon_E \tilde{e} \tag{1.70}$$

$$h = \varepsilon_p \tilde{h} \tag{1.71}$$

$$J = \varepsilon_{cost} \tilde{J} \tag{1.72}$$

In order to incorporate the scaled values into the dynamical model equations presented in Chapter II, Equations (1.9), (1.10), and (1.12), the time derivative of Equations (1.65) through (1.72) must be found. By applying the chain rule, the rate of change of the scaled states with respect to scaled time can be found as represented in Equation (1.73). Equation (1.73) is an example, showing the time derivative of Equation (1.66); similar equations are derived for all Equations (1.65) through (1.72).

$$\frac{d\tilde{\boldsymbol{\omega}}}{d\tilde{t}} = \frac{d\tilde{\boldsymbol{\omega}}}{d\boldsymbol{\omega}}\frac{d\boldsymbol{\omega}}{dt}\frac{dt}{d\tilde{t}} \tag{1.73}$$

Equations (1.9), (1.10), and (1.12) are then rewritten to include the scaled values using the required relationships defined in Equations (1.65) through (1.72) as well as their time derivatives taking the form of Equation (1.73). Equations (1.74) through (1.76) are the scaled dynamics equations.

$$\dot{\tilde{\boldsymbol{q}}} = (\frac{C\boldsymbol{\varepsilon}_\omega Q(\tilde{\boldsymbol{\omega}})\tilde{\boldsymbol{q}}}{2})\boldsymbol{\varepsilon}_q^\dagger \tag{1.74}$$

$$\dot{\tilde{\boldsymbol{\omega}}} = (\frac{J^{-1}(-C\boldsymbol{\varepsilon}_\omega\tilde{\boldsymbol{\omega}}\times(JC\boldsymbol{\varepsilon}_\omega\tilde{\boldsymbol{\omega}}+ZJ_wC\boldsymbol{\varepsilon}_\Omega\tilde{\boldsymbol{\Omega}})-ZC^2\boldsymbol{\varepsilon}_\tau\tilde{\boldsymbol{\tau}})}{C})\boldsymbol{\varepsilon}_\omega^\dagger \tag{1.75}$$

$$\dot{\tilde{\boldsymbol{\Omega}}} = (\frac{C\boldsymbol{\varepsilon}_\tau\tilde{\boldsymbol{\tau}}}{J_w})\boldsymbol{\varepsilon}_\Omega^\dagger \tag{1.76}$$

The search spaces for the quaternions, reaction wheel rotation rates, and control torques are restricted in engineering units to [-1, 1], [-1000, 1000] rpm, and [-0.2, 0.2] Nm respectively while the search space for the body rotation rates is restricted to twice its path constraint, [-0.26, 0.26] °/s. These listed values are also scaled according to Table 1 to obtain a numerical solution.

Figures 13, 14, and 15 plot the quaternions, body rotation rates, and reaction wheel rotation rates in engineering units over the time of the maneuver, illustrated with circles, along with the propagated feasibility analysis, illustrated as solid lines. Feasibility analysis uses forward propagation of the control through the dynamics, $f(\boldsymbol{x},\boldsymbol{u}) = \dot{\boldsymbol{x}}$, to find the values of each state over the maneuver duration. Feasibility analysis confirms that the numerically obtained control trajectory produces state trajectories that are feasible to the

dynamics, boundary conditions, and path constraints. Since the feasibility analysis exhibits the same trajectories as the optimal control solution (see Figures 13, 14, and 15) one feasibility condition is met. Additionally, the boundary conditions are met with reasonable accuracy as can also be seen in Figures 13, 14, and 15. Furthermore, Figure 14 shows the body rotation rate constraint of $|\omega_i(t)| \leq 0.13^\circ\!/_s$ was not violated at any point during the maneuver. Therefore, the solution can be implemented to maneuver the real spacecraft.
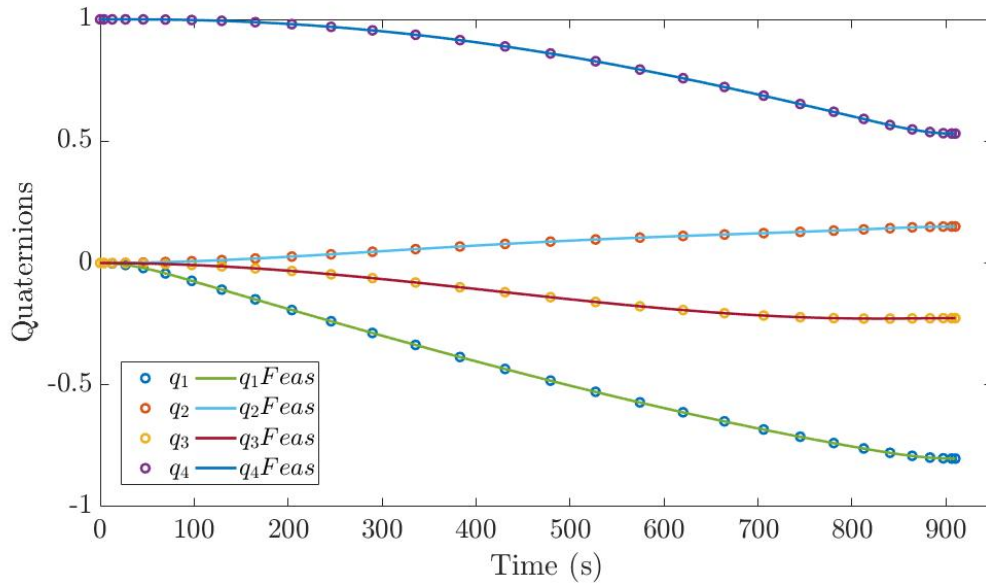

Figure 13.   Successful Feasibility of Quaternions for Minimum Electrical Energy, Fixed-Time Maneuver

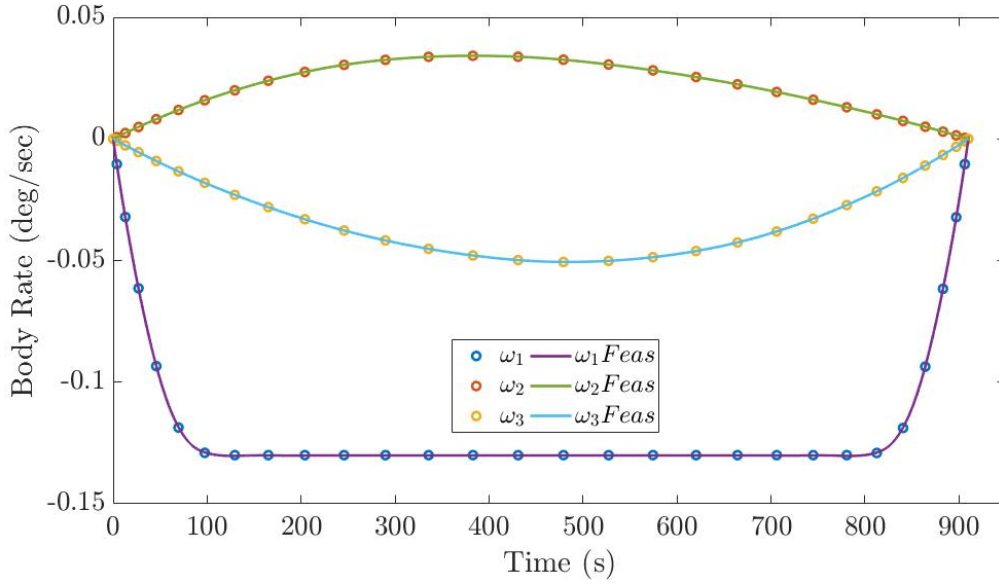Figure 14.   Successful Feasibility of Body Rotation Rates for
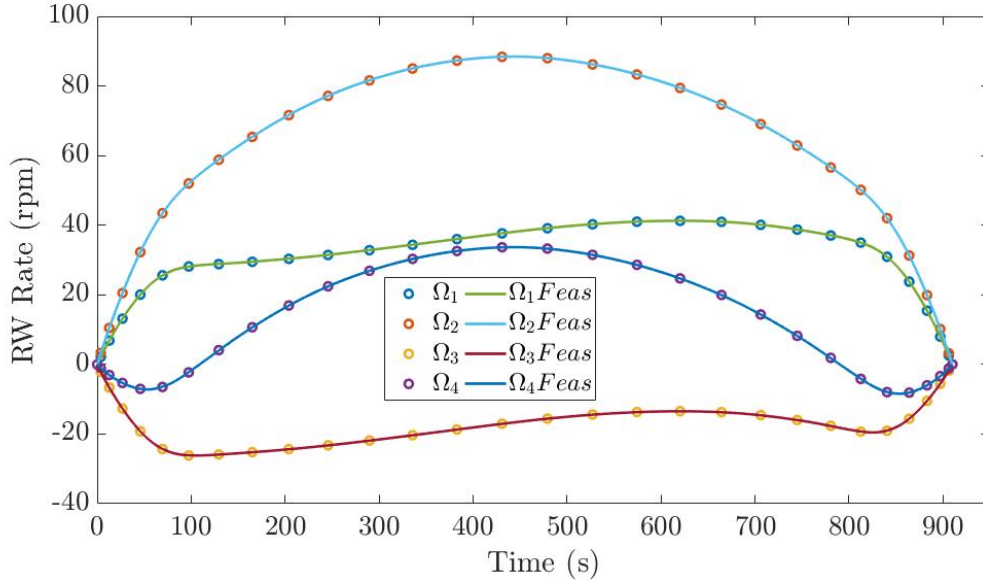Minimum Electrical Energy, Fixed-Time Maneuver

Figure 15.   Successful Feasibility of Reaction Wheel Rotation Rates
for Minimum Electrical Energy, Fixed-Time Maneuver

With the states plotted, the complementarity conditions for the body rotation rates
were checked. Application of Pontryagin's Principle stated in Equation (1.54) that μ_i

should equal zero when ω_i is between its maximum and minimum constraint value, μ_i should be greater than zero when ω_i is saturated at its maximum value, and μ_i should be less than zero when ω_i is saturated at its minimum value. Since ω_1 saturates to the minimum rotation rate, μ_1 should be less than zero during the coast period. Figure 16 confirms this behavior, showing the first covector is much less than one while the first body rotation rate is saturated. The other two body rotation rates stay between their bounds for the duration of the slew and, thus, should have zero covectors for the duration of the maneuver. Figures 17 and 18 display exactly this behavior. The complementarity conditions for the spacecraft body rotation rate states are met.

Figure 16. Satisfaction of Complementarity Condition for X-Axis Angular Rate and Covector for Minimum Electrical Energy, Fixed-Time Maneuver
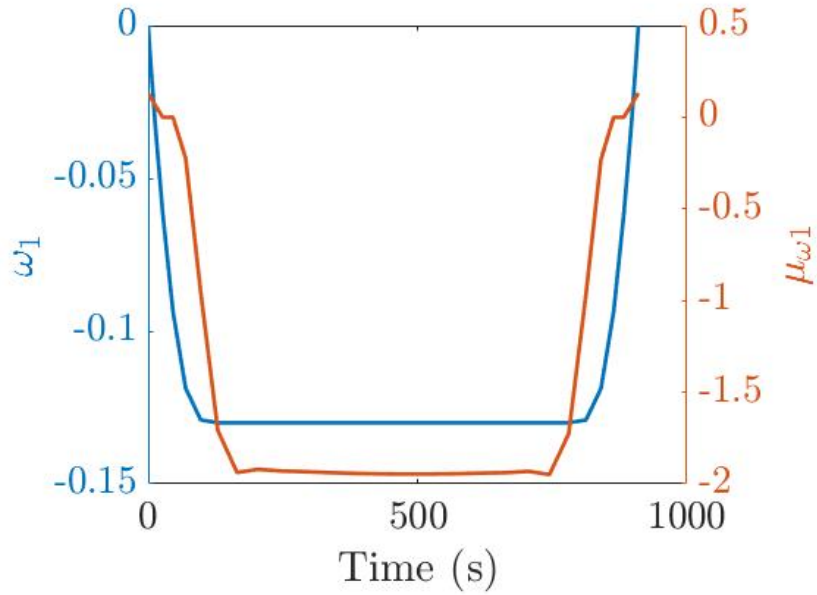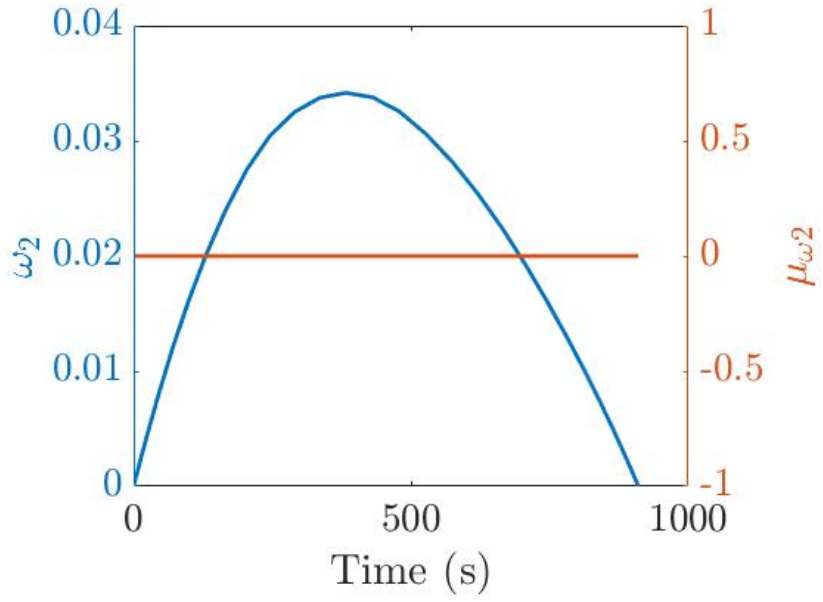
Figure 17. Satisfaction of Complementarity Condition for Y-Axis
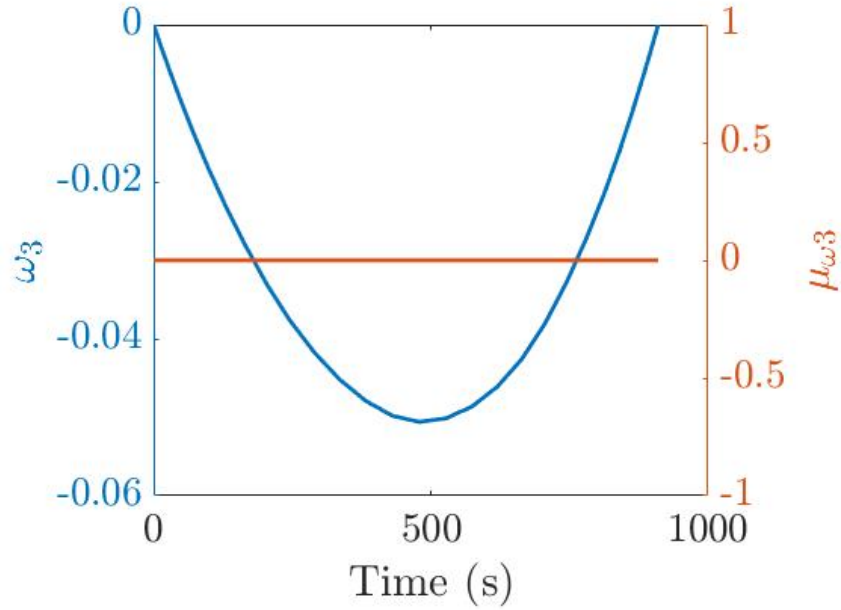Angular Rate and Covector for Minimum Electrical Energy, Fixed-Time
Maneuver

Figure 18. Satisfaction of Complementarity Condition for Z-Axis
Angular Rate and Covector for Minimum Electrical Energy, Fixed-Time
Maneuver

The control torques for an optimal electrical energy solution to an attitude control profile were expected to be much smaller throughout the maneuver in comparison to the Eigenaxis maneuver control torques due to the freedom of off-Eigenaxis maneuvering that is allowed. Furthermore, the reaction wheel control torques are expected to be non-zero for the duration of the maneuver because the maneuver solution is not restricted to be an Eigenaxis maneuver. It is apparent that this maneuver is not an Eigenaxis maneuver due to the monotonicity of the quaternion profiles shown in Figure 13 [8]. Figure 19 plots all four control torques for this MEEFT solution and shows that they fit this expected path: the Eigenaxis control torques, as shown in Figure 6, varied between $\tau = \pm 0.08 Nm$ while the MEEFT solution control torques varied by only $\tau = \pm 0.02 Nm$. Moreover, the MEEFT solution torque profiles are not equal to zero for a prolonged portion of the maneuver. Because the torque profiles match what was intuitively expected, this solution is further confirmed as a potential optimal solution.
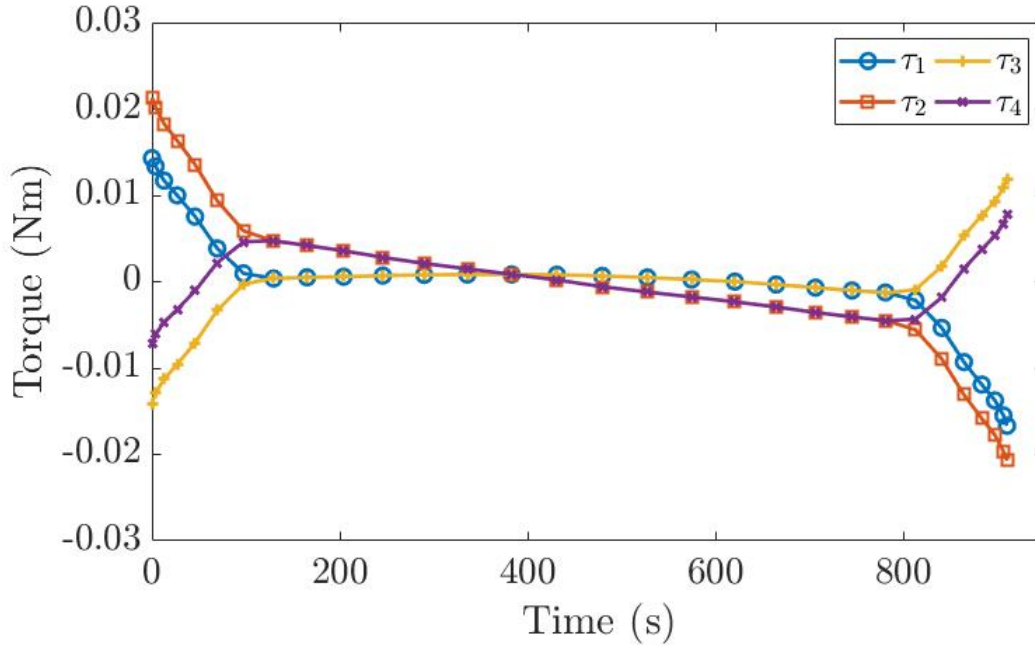

Figure 19. Control Torques for Minimum Electrical Energy, Fixed-Time Maneuver

The last critical check for this solution's optimality is the validation of the Hamiltonian Value Condition and the Hamiltonian Evolution Equation, Equations (1.58) and (1.60); the Hamiltonian should be equal to a constant for the duration of the maneuver. Because the Hamiltonian Value Condition and Hamiltonian Evolution Equation check the value of the Hamiltonian over all time, they combine to be a very powerful necessary condition that heavily suggests optimality if met. Figure 20 shows that the lower Hamiltonian does in fact meet this necessary condition: it is equal to approximately $H = -2.16$ at each time instance, only varying within ± 0.015 for the duration of the solution.
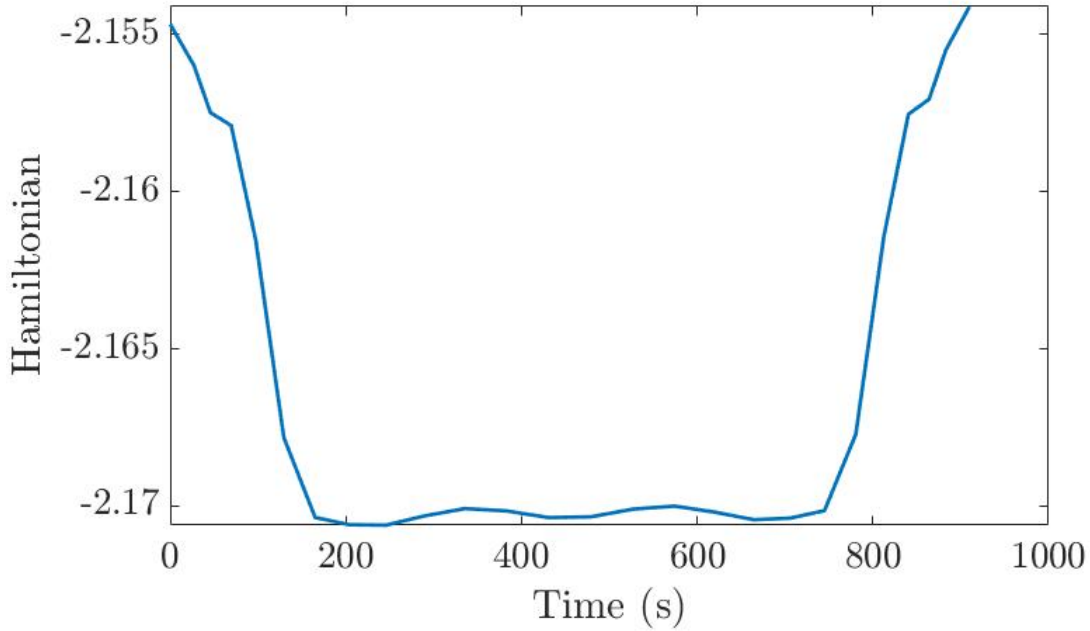
Figure 20.   Successful Validation of the Lower Hamiltonian for
Minimum Electrical Energy, Fixed-Time Maneuver

The solution should also be checked to be well balanced. If the problem is well balanced, the scaled states and related costates should vary over the same order of magnitude [25]. To illustrate the proper balancing of the scaled problem solution, the range of variation of the scaled states and costates were compared. Figures 21 through 23 show

that each state-costate pair is within one order of magnitude in scale, illustrating the problem is well scaled and balanced for an accurate numerical solution.

Figure 21.   Well Balanced Scaled Quaternions and Quaternion Costates for Minimum Electrical Energy, Fixed-Time Maneuver

Figure 22. Well Balanced Scaled Body Rotation Rates and Body Rotation Rate Costates for Minimum Electrical Energy, Fixed-Time Maneuver
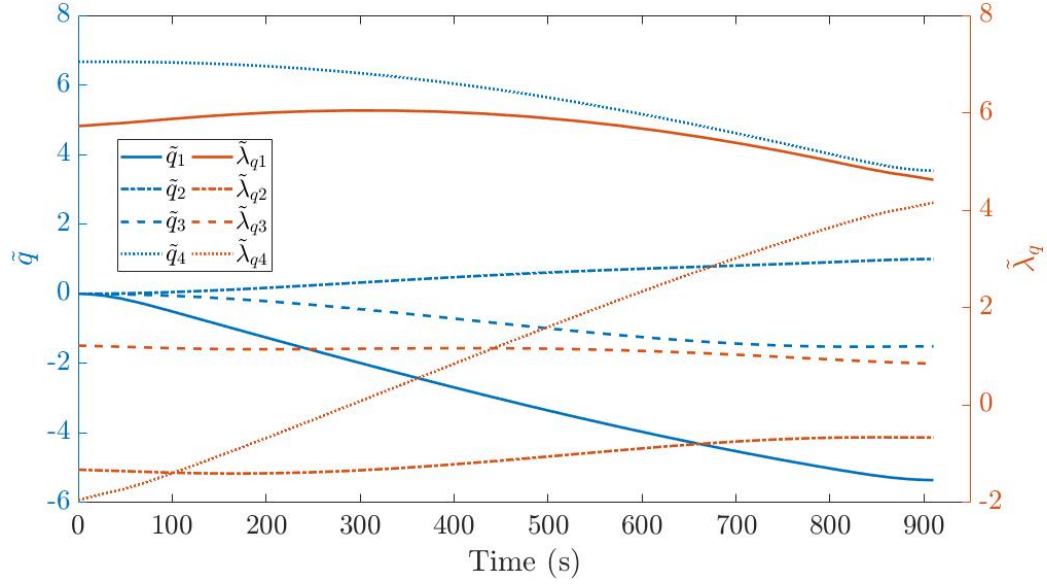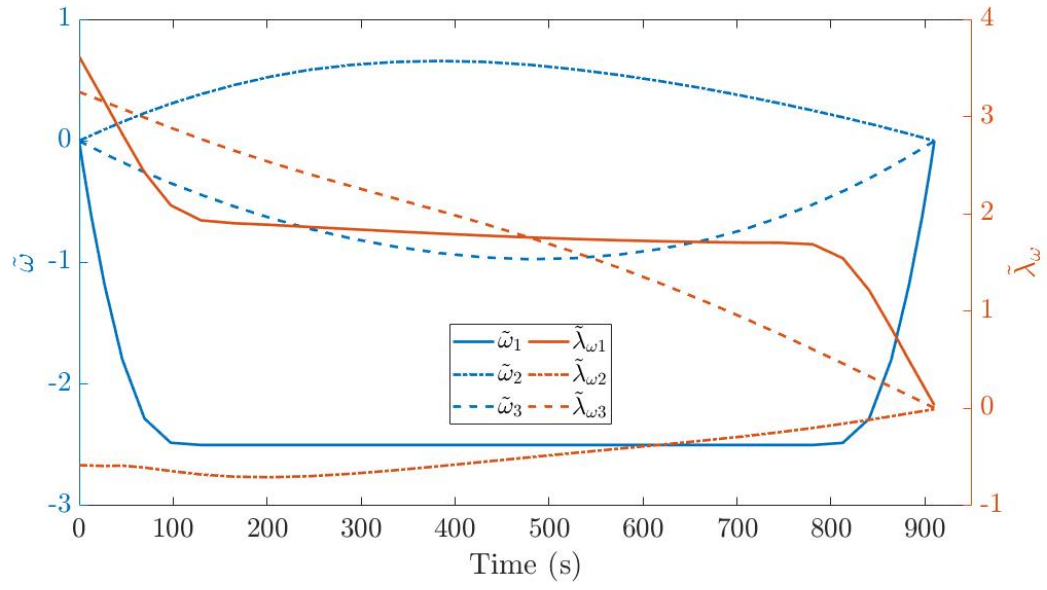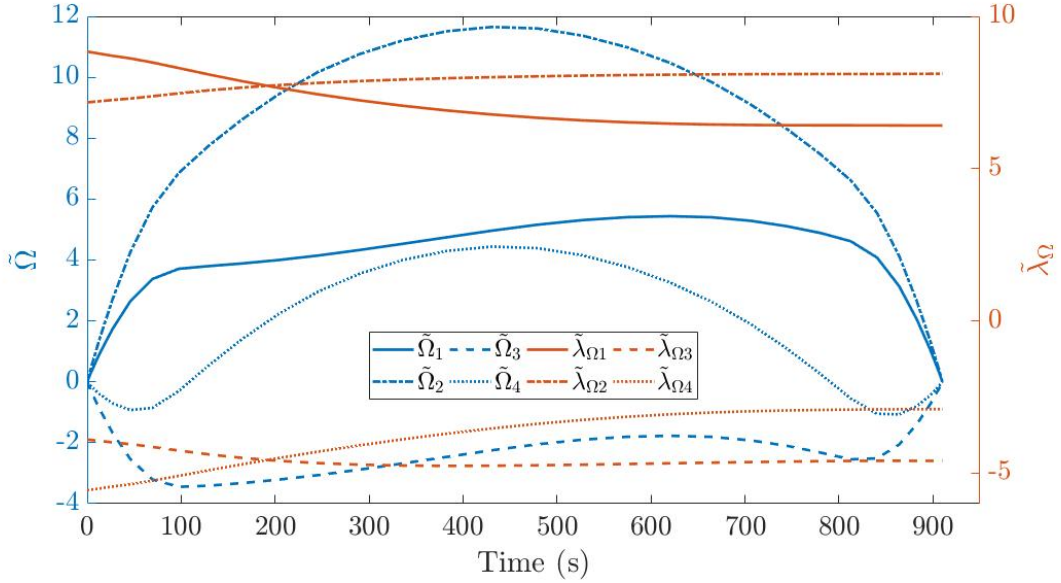

Figure 23. Well Balanced Scaled Reaction Wheel Rates and Reaction Wheel Rate Costates for Minimum Electrical Energy, Fixed-Time Maneuver

Since this solution meets the feasibility and necessary conditions and it is well balanced, it is classified as a verified optimal solution to the MEEFT problem formulation. Figure 24 shows the Eigenaxis and MEEFT maneuvers' electrical energy consumption profiles over the duration of their respective maneuver solutions while Figure 25 provides a visual representation of the Eigenaxis maneuver costs in relation to the MEEFT maneuver costs. The MEEFT maneuver requires $E = 18.35J$ of electrical energy to complete the attitude maneuver in $t_{slew} = 910s$ as compared to the standard maneuver which used $E = 28.12J$ of electrical energy in the same amount of time. The MEEFT maneuver is, therefore, the maneuver that consumes the least amount of electrical energy while completing the attitude maneuver in the same amount of time as the standard Eigenaxis maneuver. Opting for the MEEFT maneuver instead of the Eigenaxis maneuver allows an electrical energy consumption reduction of 34.7%.
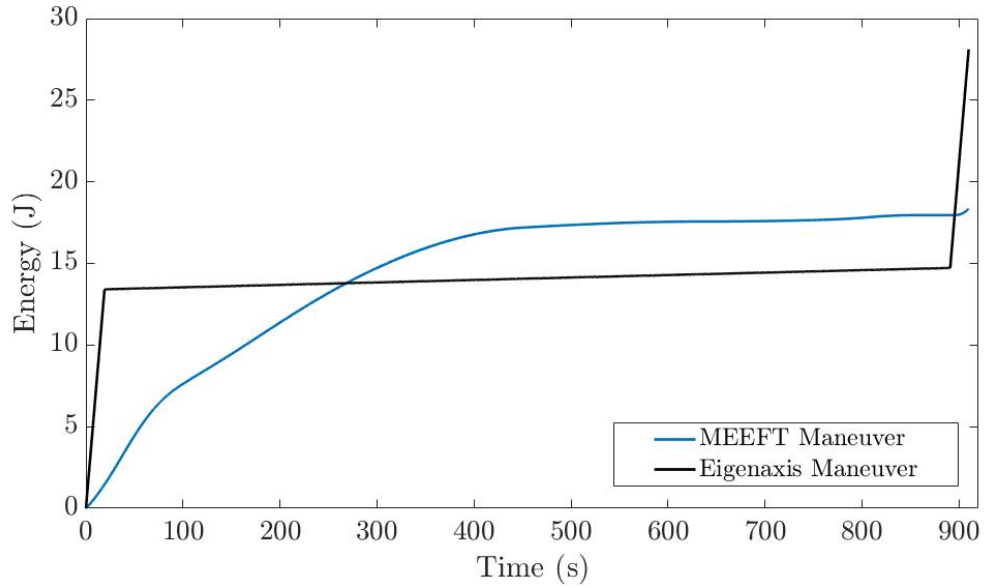
Figure 24.   Energy Consumption for Minimum Electrical Energy, Fixed-Time Maneuver
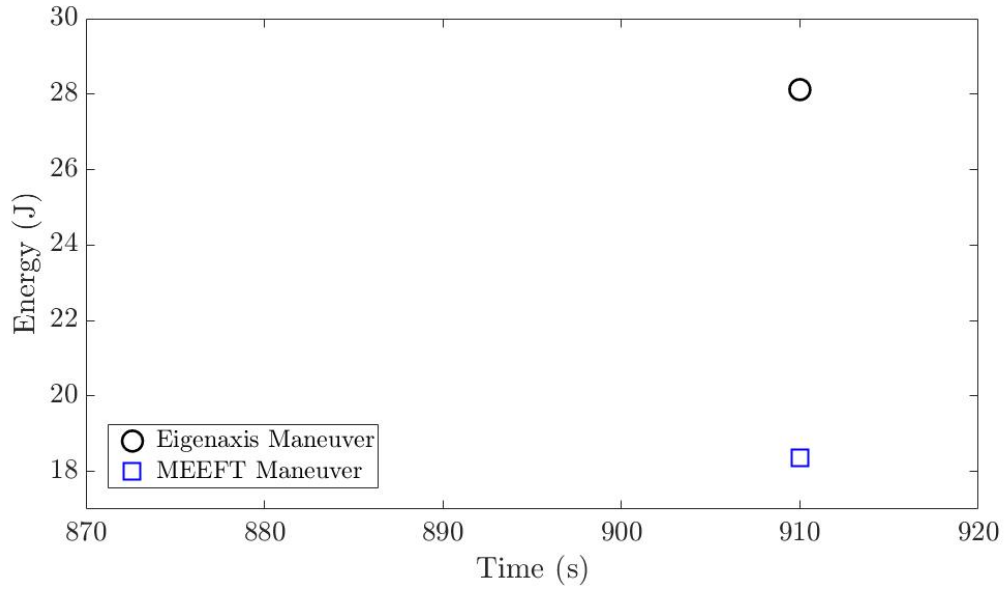
Figure 25.   Cost Comparison of Eigenaxis and Minimum Electrical
Energy, Fixed-Time Maneuver Solutions

This chapter built the MEEFT problem formulation and derived the necessary conditions for solution optimality. The MEEFT maneuver solution was identified as meeting the necessary conditions for optimality and was shown to consume less electrical energy to complete the same maneuver as the Eigenaxis maneuver. To completely characterize the corners of the conceptual optimal maneuver operating envelope for this maneuver in Figure 10, the next chapter builds and numerically solves a problem formulation for a maneuver that will consume the same electrical energy as the Eigenaxis maneuver but complete in less time.

THIS PAGE INTENTIONALLY LEFT BLANK

V. EQUIVALENT ELECTRICAL ENERGY, REDUCED TIME (EEERT) MANEUVER

This chapter will present the EEERT maneuver, a trajectory solution that will consume an equivalent amount of electrical energy but is expected to complete in a shorter time than the Eigenaxis maneuver as illustrated in Figure 26 based off of [3]. The EEERT maneuver is highlighted in the conceptual maneuver design trade space in Figure 26. The EEERT maneuver was found via iterating the MEEFT problem formulation through DIDO with decreasing fixed times until a solution was found that consumed an equivalent amount of electrical energy as the original Eigenaxis maneuver. A plot of energy versus time can also be made from these solutions to provide a lower bound on the energy-time trade space. The identified optimal solution will be presented and this chapter will conclude with the time and electrical energy costs of the EEERT maneuver.
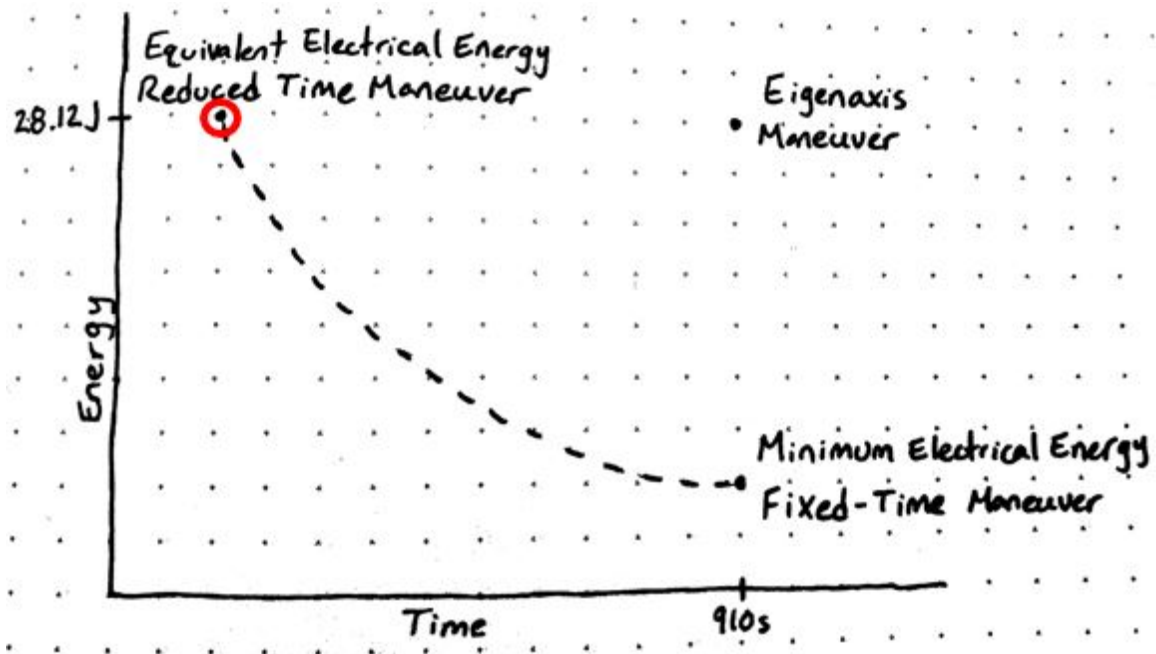

Figure 26.   Conceptual Cost Relation Between Equivalent Electrical
Energy, Reduced Time Maneuver and Eigenaxis Maneuver

A.   EEERT PROBLEM FORMULATION AND NECESSARY CONDITIONS FOR OPTIMALITY

The problem formulation used to find the EEERT maneuver is identical to the MEEFT problem formulation with the exception of the specification of the final time. The specific value of the final time was decreased iteratively every five seconds until the electrical energy cost was equal to $E = 28.12J$ (the cost associated with the Eigenaxis slew). The EEERT maneuver solution had a final time of $t_{slew} = 872s$.

Because the EEERT problem formulation is exactly the same for the MEEFT problem formulation (see Chapter IV) with only a change to the final fixed time, the feasibility and necessary conditions are identical. To be an optimal solution, the EEERT maneuver solution must meet feasibility analysis, all boundary conditions, and it must be well scaled and balanced. The necessary conditions that will be tested include the Complementarity Conditions in Equation (1.54) along with the Hamiltonian Value Condition and Hamiltonian Evolution Equation conditions in Equations (1.58) and (1.60), respectively.

B.   EEERT NUMERICAL SOLUTION

With the EEERT problem formulation built and the feasibility and necessary conditions identified, the solution will be presented in this section. The EEERT solution was produced using the same canonical and designer unit scaling as presented in Table 1. It was not necessary to make any adjustments to these scaling values. The search spaces for the quaternions, reaction wheel rotation rates, control torques, and body rotation rates were kept the same as the ones used to solve MEEFT problem formulation.

Figures 27, 28, and 29 plot the quaternions, body rotation rates, and reaction wheel rotation rates over the duration of the slew in engineering units, illustrated with circles, along with the propagated state trajectories, illustrated as solid lines. Since the propagated states run along the trajectories of the numerical solution in Figures 27, 28, and 29, the EEERT solution meets the feasibility condition. Figures 27, 28, and 29 also show the plotted EEERT solution meets the boundary conditions well, satisfying another feasibility condition. Also of note, Figure 28 shows the body rotation rate constraint of

$|\omega_i(t)| \leq 0.13 \frac{\circ}{s}$ was satisfied for all time during the EEERT maneuver as a consequence of the path constraint implemented as part of the EEERT problem formulation.

Figure 27. Successful Feasibility of Quaternions for Equivalent
Electrical Energy, Reduced Time Maneuver

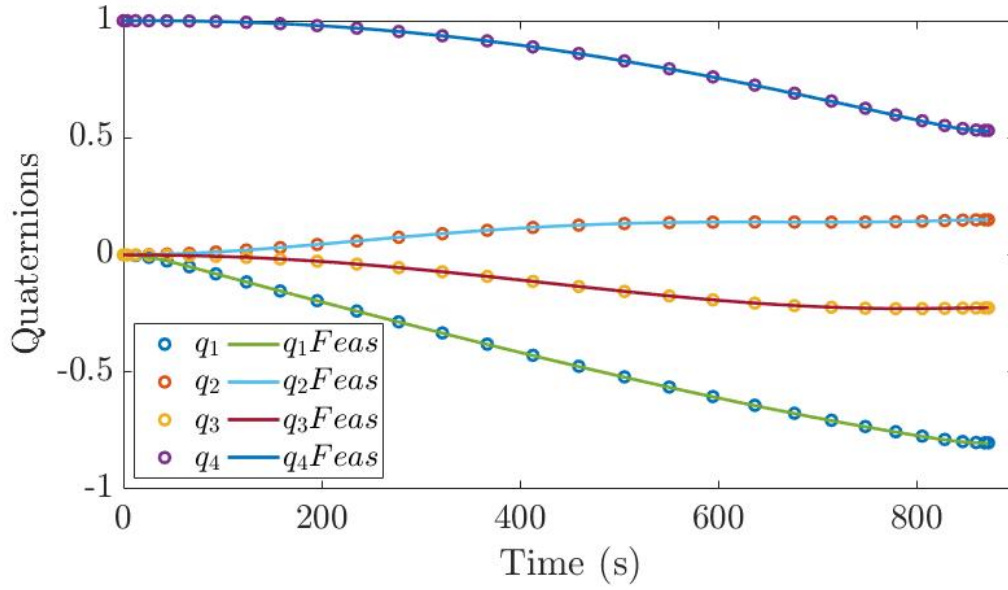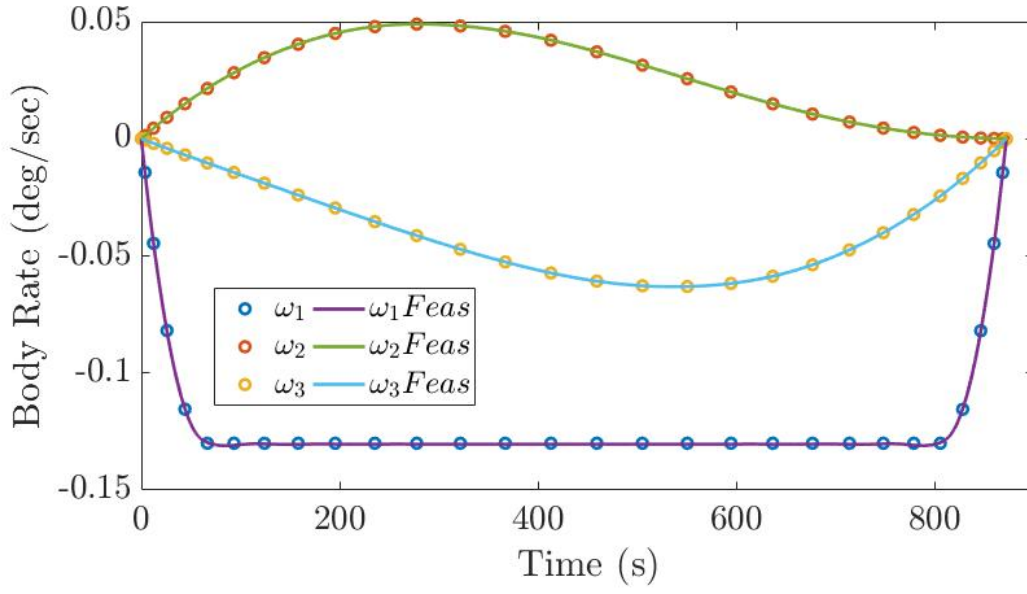Figure 28. Successful Feasibility of Body Rotation Rates for
Equivalent Electrical Energy, Reduced Time Maneuver
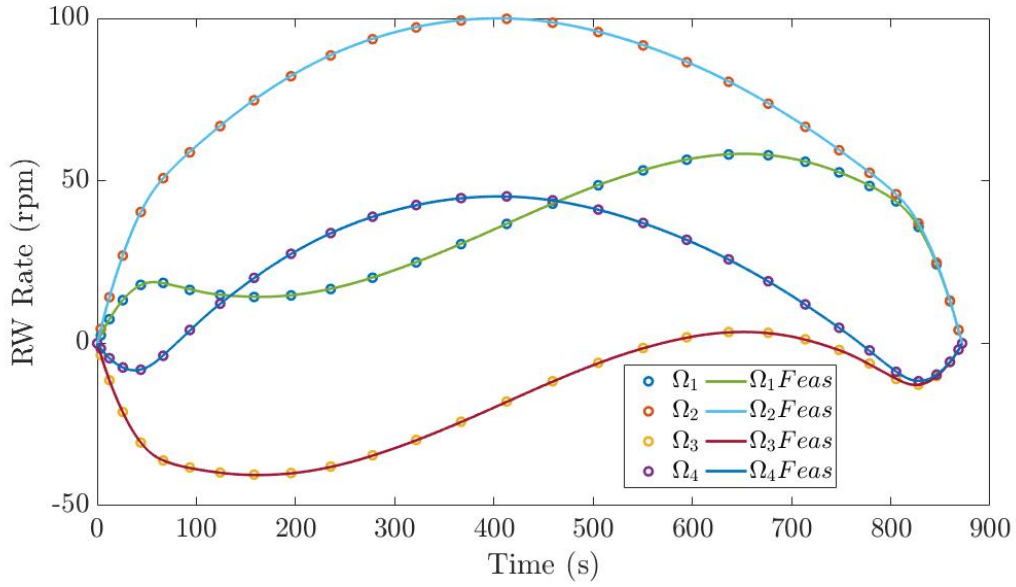
Figure 29. Successful Feasibility of Reaction Wheel Rotation Rates
for Equivalent Electrical Energy, Reduced Time Maneuver

The complementarity conditions for P$_{EEERT}$ were checked once the states were
identified as passing feasibility analysis. Just like for the MEEFT maneuver, μ_i should

equal zero when ω_i is between its maximum and minimum constraint value, μ_i should be greater than zero when ω_i is saturated at its maximum value, and μ_i should be less than zero when ω_i is saturated at its minimum value. Since ω_1 is the only body rotation rate to reach its minimum saturation limit for a portion of the maneuver, μ_1 should be less than zero for that same portion while the other two covectors remain equal to zero. Figures 30, 31, and 32 confirm this EEERT solution exhibits this behavior.

Figure 30. Satisfaction of Complementarity Condition for X-Axis Angular Rate and Covector for Equivalent Electrical Energy, Reduced Time Maneuver
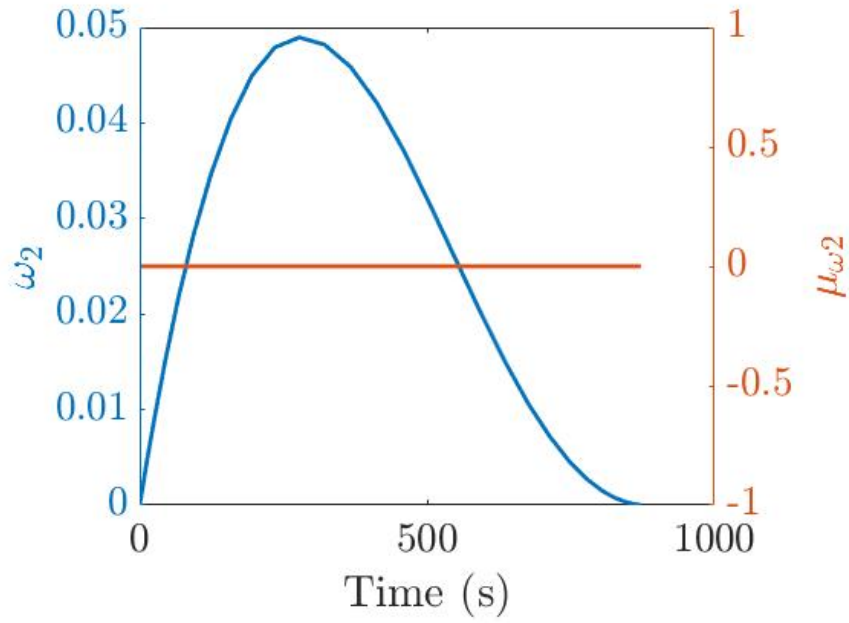
Figure 31. Satisfaction of Complementarity Condition for Y-Axis
Angular Rate and Covector for Equivalent Electrical Energy, Reduced Time
Maneuver
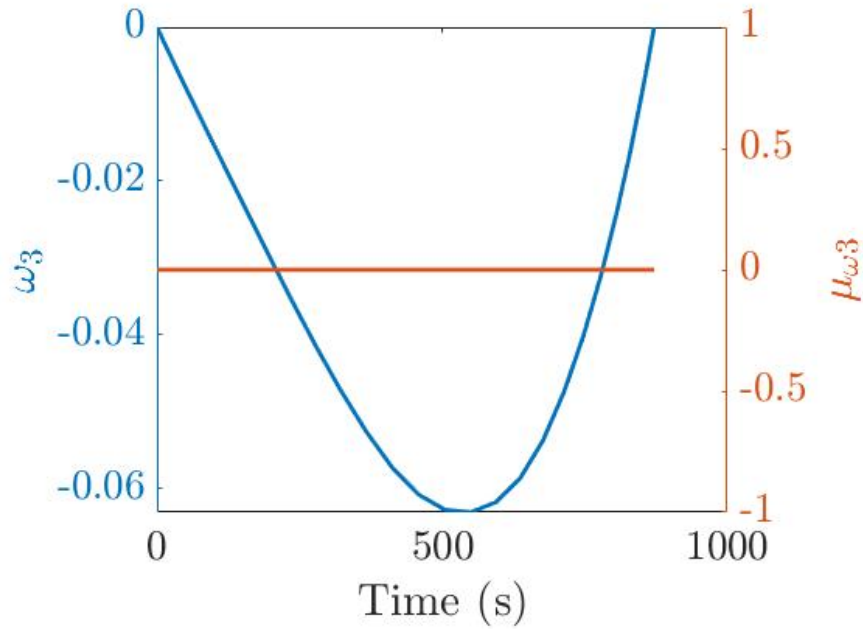
Figure 32. Satisfaction of Complementarity Condition for Z-Axis
Angular Rate and Covector for Equivalent Electrical Energy, Reduced Time
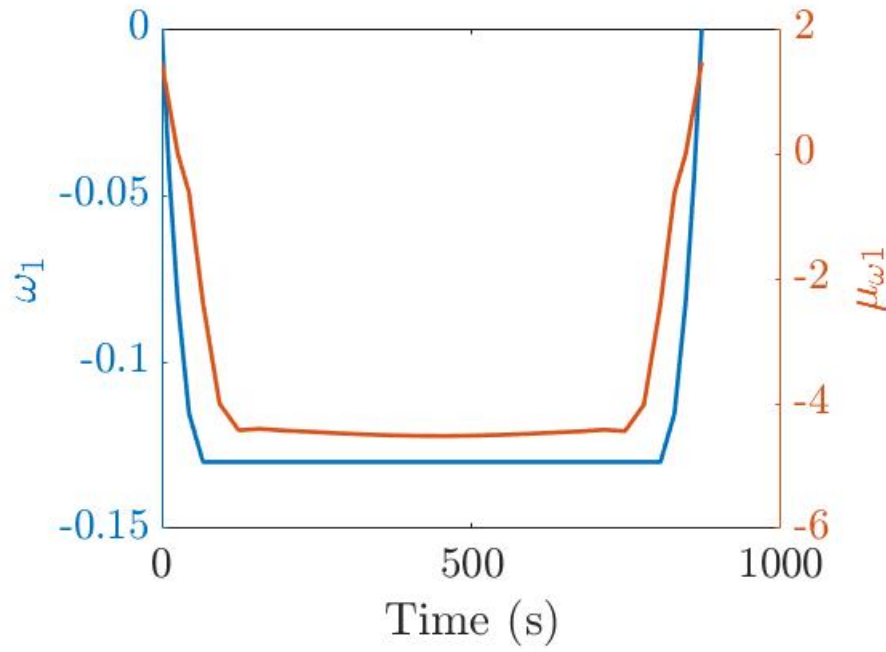Maneuver

50

The EEERT control torque profiles are expected to be relatively higher than the MEEFT control torques as would be required to rotate the spacecraft body at a faster rate. Similar to the MEEFT maneuver control torques, the EEERT reaction wheel control torques are expected to be non-zero for the duration of the maneuver since the EEERT maneuver solution is not an Eigenaxis maneuver due to the monotonicity of its quaternion profiles shown in Figure 27 [8]. Figure 33 plots all four control torques for the EEERT solution and illustrates the torques do reasonably fit the expected profile: the EEERT torques vary between $\tau = \pm 0.03 Nm$ which is larger than the MEEFT torques at $\tau = \pm 0.02 Nm$ but smaller than the Eigenaxis torques at $\tau = \pm 0.08 Nm$.
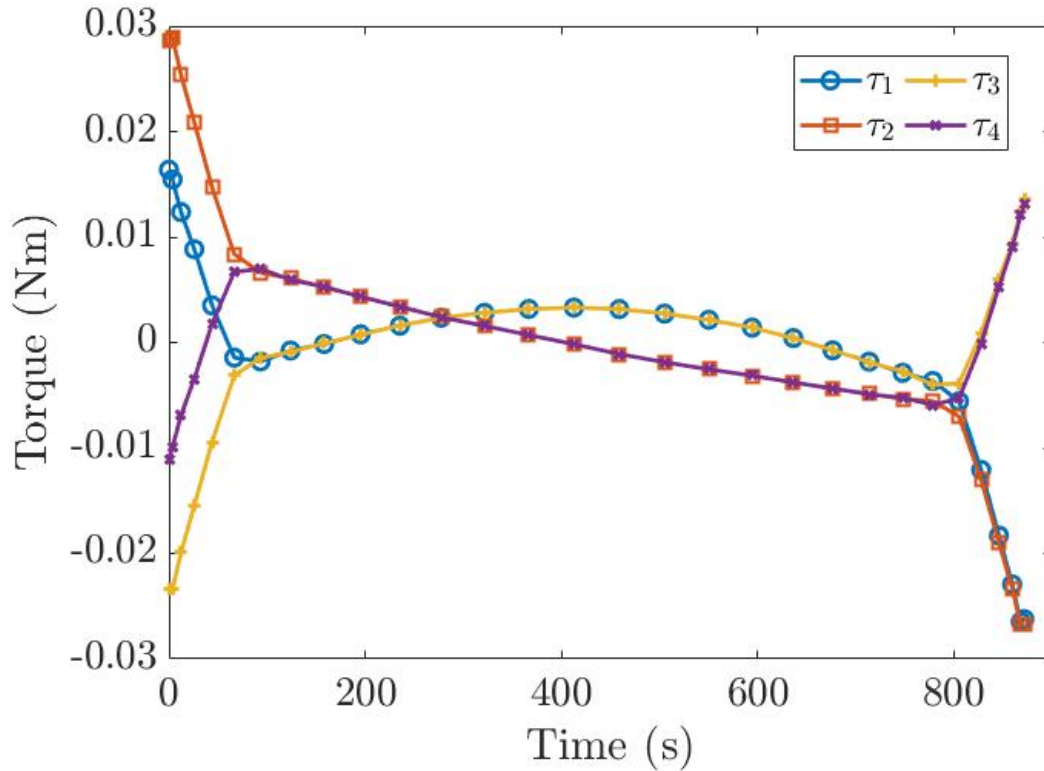
Figure 33. Control Torques for Equivalent Electrical Energy, Reduced Time Maneuver

The last critical necessary conditions to check to validate the optimality of the solution are the Hamiltonian Value Condition and the Hamiltonian Evolution Equation.

Figure 34 shows that the lower Hamiltonian satisfies both necessary conditions, being equal to an undetermined constant for all time (the Hamiltonian varies by ± 0.05 around $H = -4.87$ which is well within error norms). With this, the EEERT maneuver solution meets all the necessary conditions to be considered an optimal solution.
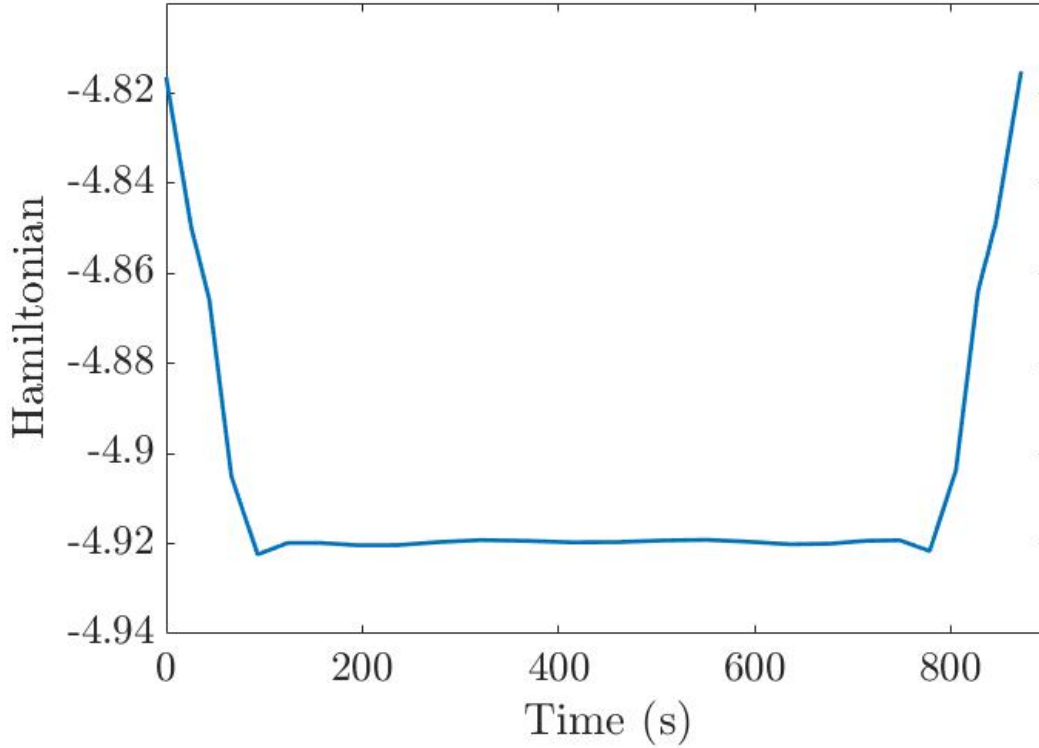
Figure 34.   Hamiltonian for Equivalent Electrical Energy, Reduced Time Maneuver

Now that the EEERT maneuver is confirmed to be an optimal solution, the EEERT maneuver solution's balancing is checked. If the problem is well balanced, the scaled states and related costates should vary within one order of magnitude [25]. Figures 35 through 37 show that the scaling used yields a well-balanced problem.

52
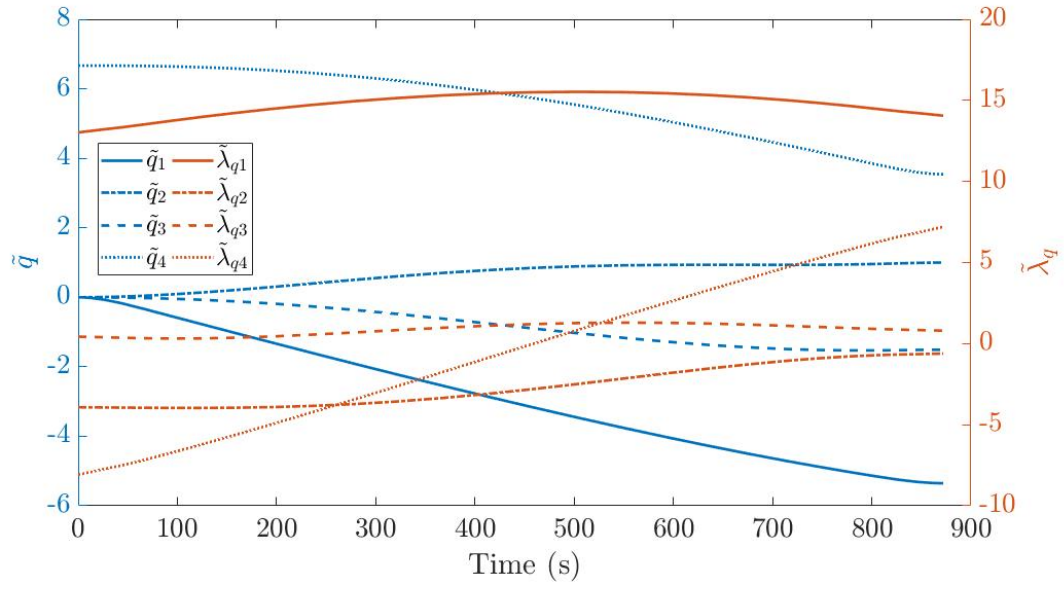
Figure 35.   Well Balanced Scaled Quaternions and Quaternion
Costates for Equivalent Electrical Energy, Reduced Time Maneuver
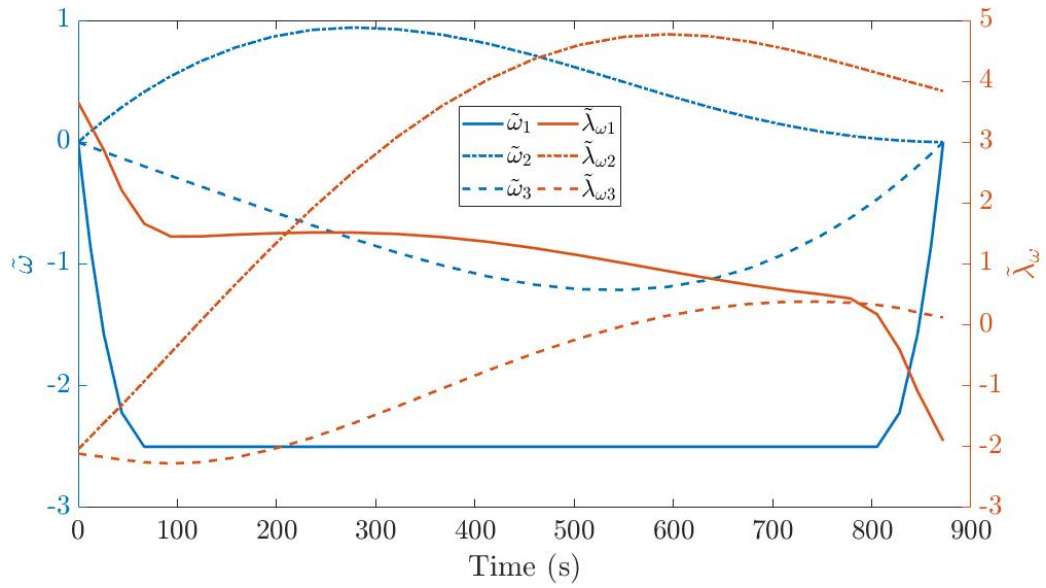
Figure 36.   Well Balanced Scaled Body Rotation Rates and Body
Rotation Rate Costates for Equivalent Electrical Energy, Reduced Time
Maneuver

53
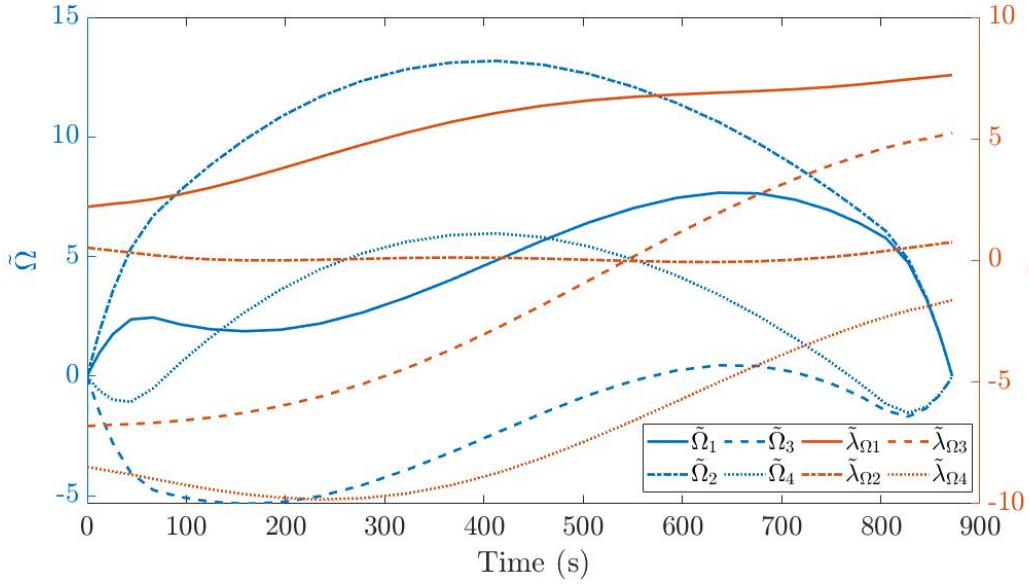
Figure 37. Well Balanced Scaled Reaction Wheel Rates and Reaction Wheel Rate Costates for Equivalent Electrical Energy, Reduced Time Maneuver

Since the EEERT maneuver solution of this chapter a) meets the feasibility and necessary conditions, b) consumes the same amount of electrical energy as the Eigenaxis maneuver, and c) completes the slew in less time, the solution may be classified as an optimal solution to the EEERT problem formulation. This EEERT maneuver costs $E = 28.12J$ of electrical energy and completes the slew in $t_{slew} = 872s$. Figure 38 shows the Eigenaxis, MEEFT, and EEERT maneuvers' electrical energy consumption profiles over the duration of their maneuver solutions.
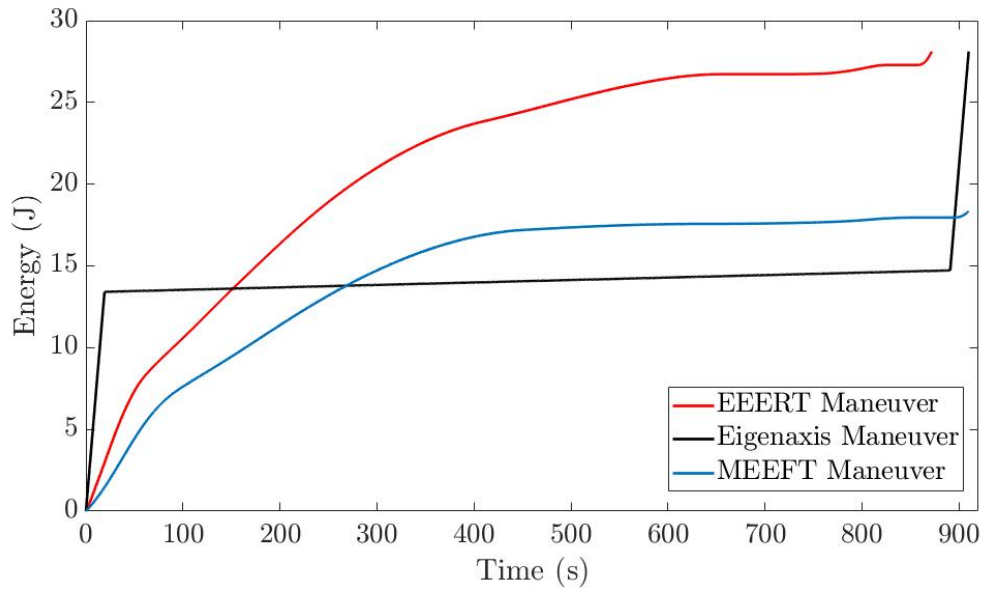
Figure 38.   Cost Comparison of Standard and Two Different Optimal
Maneuver Solutions

Figure 39 plots the EEERT maneuver costs in relation to both the MEEFT and Eigenaxis maneuver costs, constructing an electrical energy - time cost tradespace for the particular maneuver studied in this thesis. Although graphically similar to the tradespace created in [3], Figure 39's tradespace is created for a spacecraft with extremely limiting parameters and, thus, is unique to the community. An operating envelope such as this tradespace gives mission planners and spacecraft operators a number of attitude maneuver solutions to choose from when designing a spacecraft's maneuvers. Providing this tradespace suddenly reveals an opportunity to determine a critical cost to minimize, allowing a spacecraft's mission to be more finely tailored to its particular systems. If a spacecraft has a smaller power margin, choosing maneuvers that minimize electrical energy consumption could be chosen. If time is of essence for the spacecraft's mission, a minimum time slew could be chosen out of the tradespace created for this particular maneuver. If both electrical energy and time need to be conserved, a trajectory with costs existing within the boundaries of the tradespace in Figure 39 could be designed and flown. This operating envelope, as well as others like it that could be developed for other

maneuver endpoints, provides flexibility for mission planners and spacecraft operators working to maximize the amount of collected data from the spacecraft on orbit.
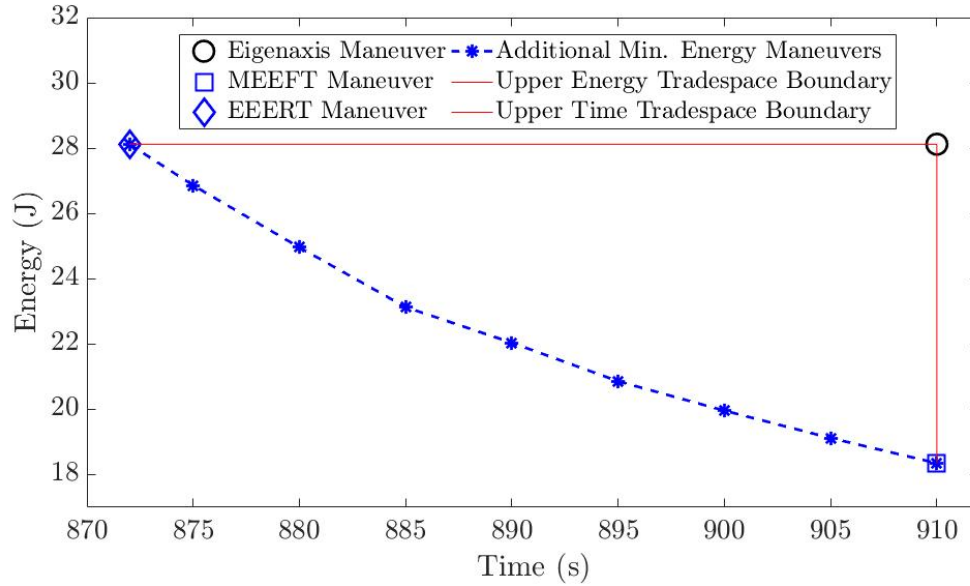
Figure 39.   Electrical Energy – Time Tradespace for Example Slew
Maneuver

Chapter V built the EEERT problem formulation and identified the necessary conditions for optimality. The chapter numerically solved and validated the EEERT maneuver and, upon confirming the EEERT solution as optimal, constructed a maneuver cost tradespace with the Eigenaxis and MEEFT trajectory costs presented earlier within this thesis in Chapters III and IV. Building this tradespace in Figure 39 completes the first objective of this thesis. To further justify the importance of the electrical energy – time tradespace relationship, the next chapter sets out to empirically validate the power model used through a live testbed. Chapter VI goes on to conduct this validation, an analysis that has never been completed before.

VI.   EMPIRICAL VALIDATION OF THEORETICAL RESULTS

With the industry standard maneuver, electrical energy saving maneuver, and agile electrical energy equivalent maneuver all determined and their theoretical electrical energy costs computed, an experiment to validate the power model used in the preceding analysis was created. Experimental evaluation of a maneuver's electrical energy consumption provides concrete evidence that results determined through numerical work holds or does not hold in practice. Ideally, the three found maneuvers would be tested on a reaction wheel testbed with the same characteristics and constants as the spacecraft modeled in this research; this would allow the maneuvers to be tested as they have been presented. The Naval Postgraduate School does not have access to an attitude control system testbed with reaction wheels that match the specifications used earlier. Nonetheless, the Naval Postgraduate School does have a reaction wheel testbed compromising a set of smaller reaction wheels. This reaction wheel testbed can be used to check Equation (1.14) if the electrical power draw and resulting electrical energy consumption for each maneuver is recalculated for the alternative set of reaction wheels. This chapter will present the physical characteristics of the laboratory testbed and recompute the expected electrical energy consumption of the Eigenaxis, MEEFT, and EEERT Maneuvers for this particular system. This chapter will continue to describe the testbed hardware setup as well as the software versions and codes developed in order to record the empirical data on power. Finally, this chapter will document the test procedures used to collect the data before presenting the test results.

A.   PREDICTED POWER CONSUMPTION

The Naval Postgraduate School's Control & Optimization Laboratory reaction wheel testbed consists of four reaction wheels based on a Maxon EC-Motor actuator [17]. Each wheel is a 90W, brushless drive that runs at a nominal voltage of 24V, produces a nominal torque of 0.44 Nm, and has a maximum rotation rate of 5000 rpm. The terminal resistance and torque constant for these wheels was used in the Eigenaxis, MEEFT, and EEERT maneuver derivations as explained in Chapter II, as the values are similar to the

larger reaction wheel values found on the modeled spacecraft. The major difference in the reaction wheel model used to generate the three maneuvers in Chapters III, IV, and V versus the reaction wheel hardware tested within this chapter is the reaction wheels' rotational inertia which affects the scale of applied torque. The inertia of the laboratory reaction wheel set is $J_m = 0.000306 kg \cdot m^2$. In order to properly scale the applied torques, Equation (1.77) was used to match the reaction wheel accelerations.

$$\tau_m = \frac{J_m}{J_w} G\tau \qquad (1.77)$$

where τ_m is the applied motor torque and G is an arbitrarily chosen factor used to scale up the operational range of the laboratory reaction wheels. For the experiments presented in this thesis, G was selected as $G = 15$.

Since the applied torques were scaled, the commanded reaction wheel rotation rates also need to be scaled by the same factor; Equation (1.78) accomplished this.

$$\mathbf{\Omega}_m = G\mathbf{\Omega} \qquad (1.78)$$

The reaction wheel applied torques and rotation rates from the Eigenaxis maneuver, the MEEFT maneuver, and the EEERT maneuver were inserted into Equation (1.77) and Equation (1.78) to produce the appropriate applied torques and commanded reaction wheel rotation rates for each maneuver to be implemented on the experimental testbed. The τ_m and $\mathbf{\Omega}_m$ values for each maneuver were then used with the power model (Equation (1.14)) in order to find the electrical power draw of each maneuver when run with the testbed's reaction wheel system. The results are given in Figures 40 through 42.
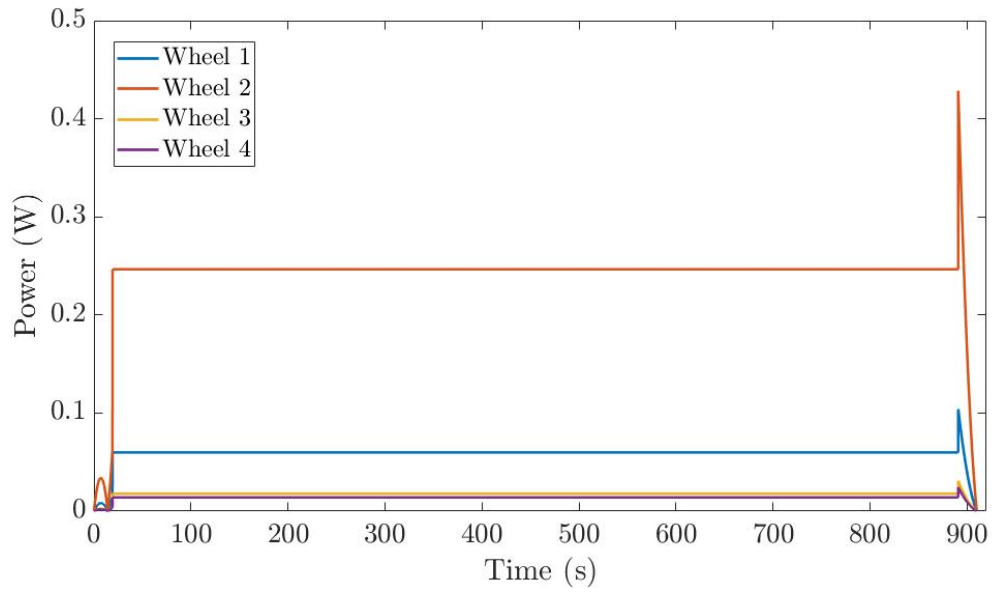
Figure 40.   Predicted Electrical Power Draw for Eigenaxis Maneuver
on Laboratory Testbed

Figure 41.   Predicted Electrical Power Draw for Minimum Electrical
Energy, Fixed-Time Maneuver on Laboratory Testbed

Figure 42.   Predicted Electrical Power Draw for Equivalent Electrical
Energy, Reduced Time Maneuver on Laboratory Testbed

Integrating the individual reaction wheel power curves built from Equations (1.77) and (1.78) and summing them gave the expected electrical energy consumption of each maneuver when run on the testbed. The expected electrical energy consumption for each maneuver is plotted in Figures 43 through 45. Figures 44 and 45 show the predicted electrical energy consumption for the two optimally designed maneuvers are each higher than the Eigenaxis Maneuver when mapped to the testbed reaction wheel system. This is because the recalculated power curves are dominated by friction losses and do not accurately reflect the mechanical power needed to perform the slew. Despite the fact that the two optimally designed maneuvers require a larger power draw on the testbed reaction wheel system, the two maneuver profiles are useful to validate the power model. As long as the collected power data reasonably matches the predicted power draw and electrical energy consumption figures here, the power model can be tested.
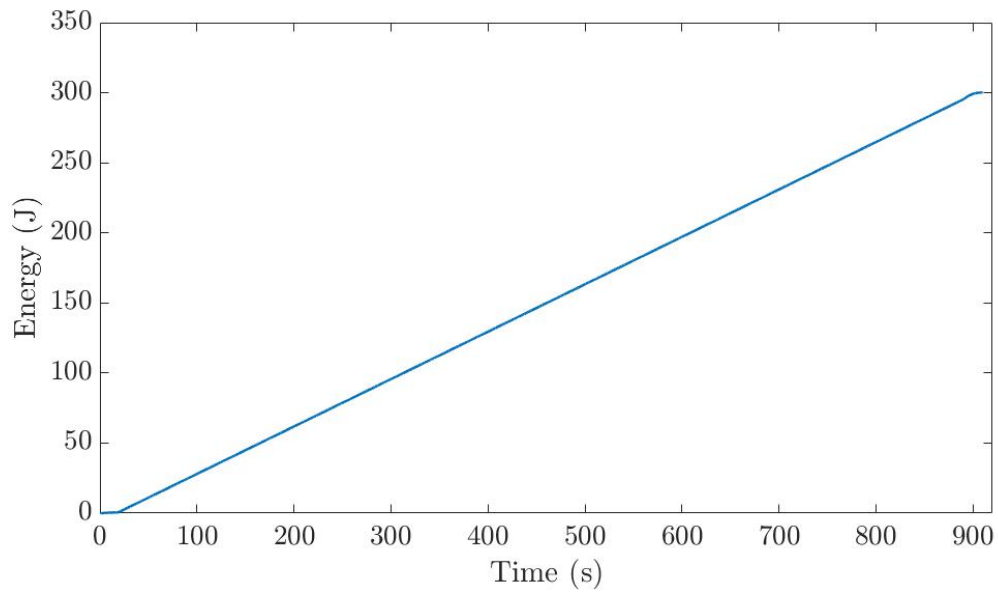
Figure 43.   Predicted Electrical Energy Consumption for Eigenaxis
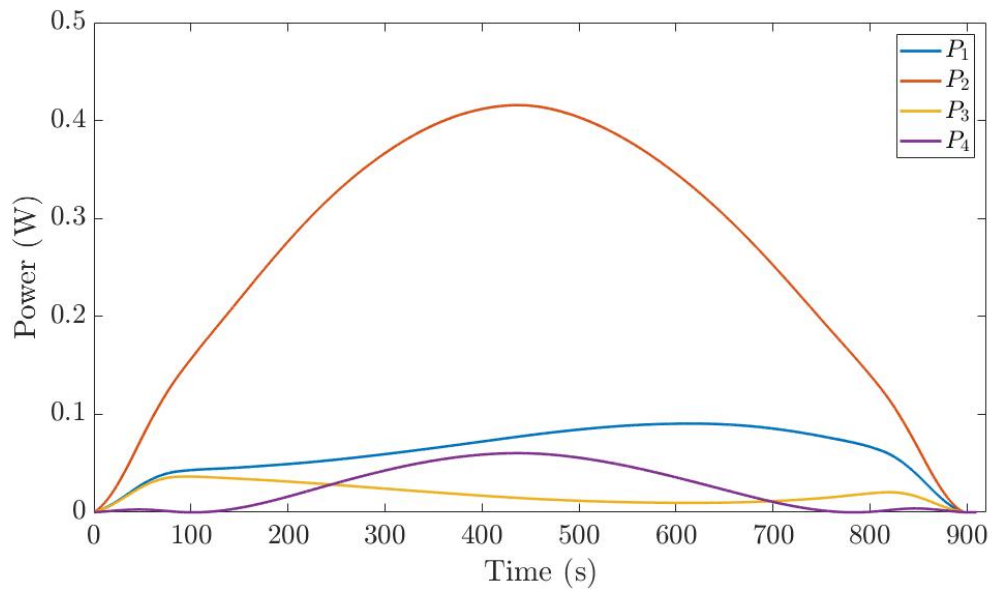Maneuver on Laboratory Testbed
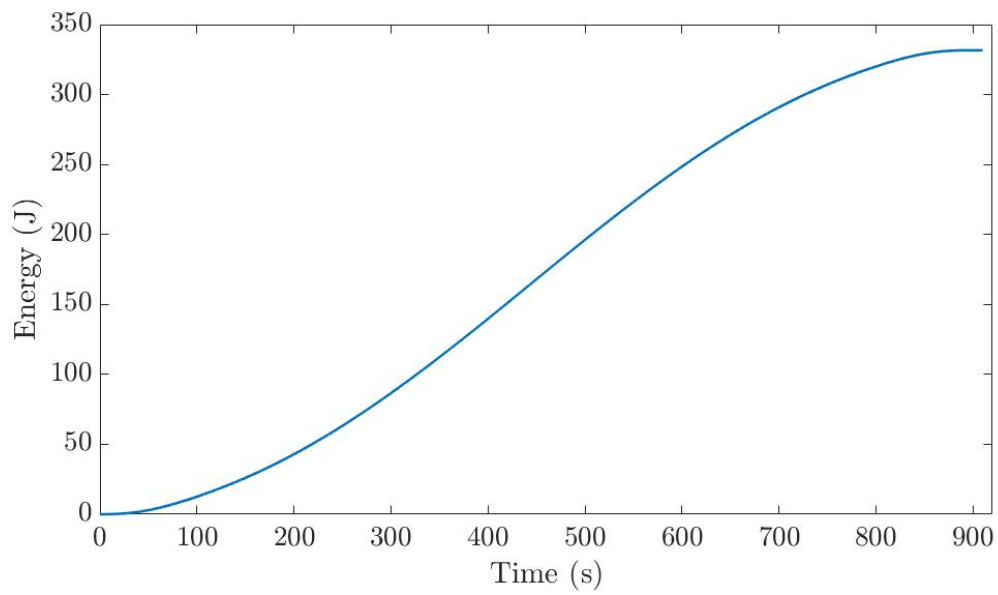
Figure 44.   Predicted Electrical Energy Consumption for Minimum
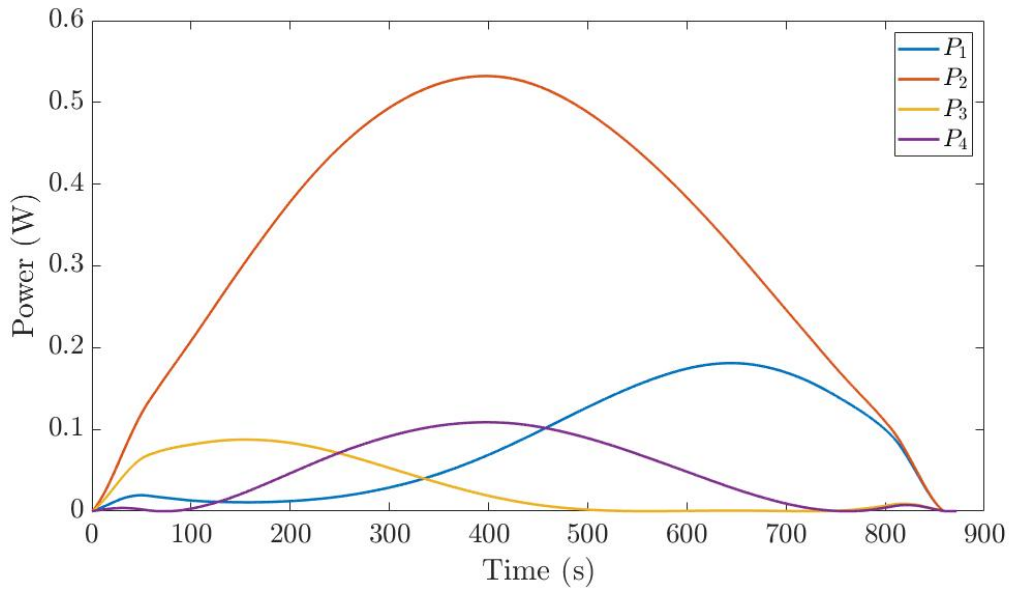Electrical Energy, Fixed-Time Maneuver on Laboratory Testbed
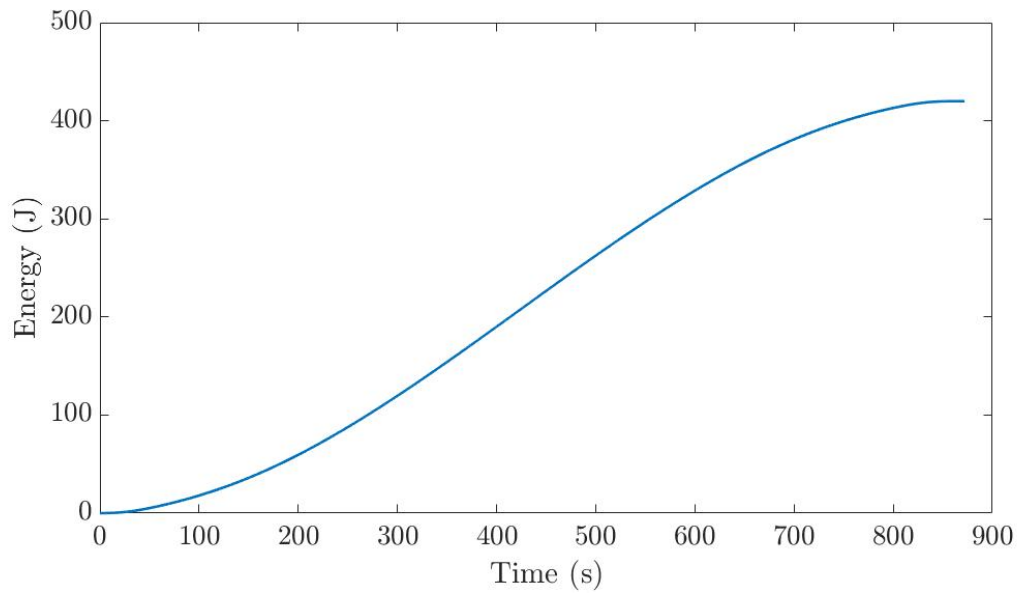
Figure 45.   Predicted Electrical Energy Consumption for Equivalent
Electrical Energy, Reduced Time Maneuver on Laboratory Testbed

B.   TESTBED SETUP

Before the experiment results can be presented, the remaining hardware and
software components of the testbed must be described. This attitude control system testbed
featured a power source, four reaction wheels, their respective motor controllers, an inline
current sensor, an analog signal reader, and a central command computer as shown in
Figure 46.
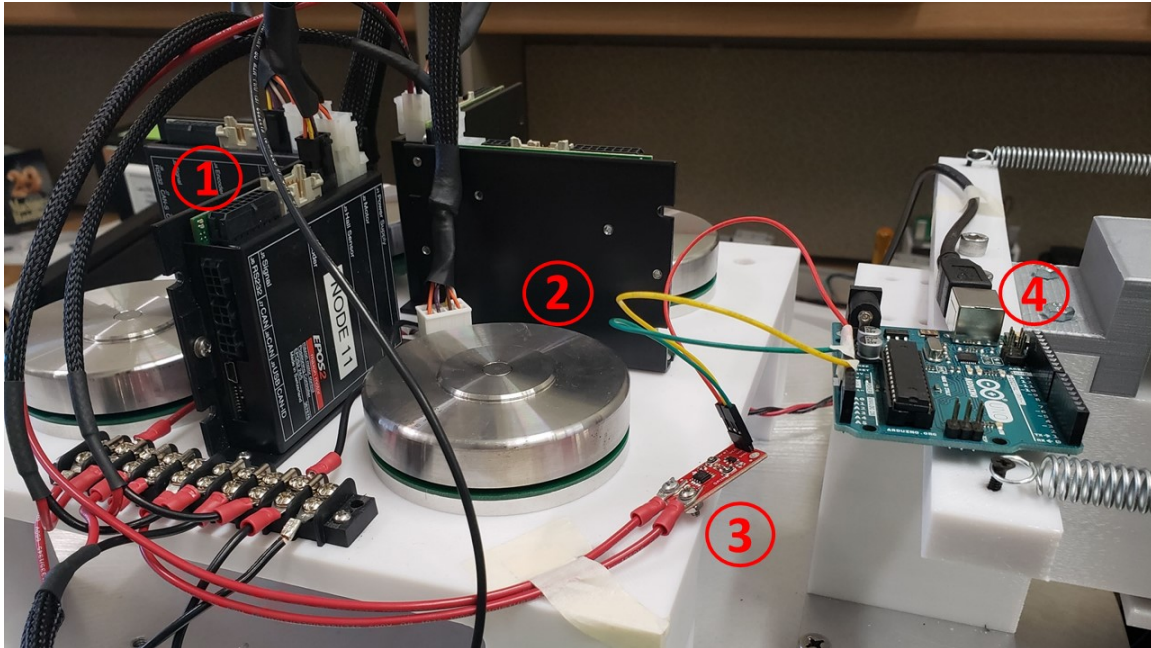
Legend: 1) EPOS Control Nodes; 2) Maxon Motor Reaction Wheels; 3) Sparkfun Low Current Sensor; 4) Arduino Uno

Figure 46.   Reaction Wheel Testbed

The four reaction wheels are based on Maxon Motor's flat, 90mm, EC brushless motors with hall sensors [19]. Each motor was commanded by an EPOS 2 24/5 digital positioning controller [26]. The EPOS controllers were connected to the central computer via RS232 cables. The current sensor was a Sparkfun ACS723 Low Current sensor capable of detecting currents between 10mA to 5A [27]. The current sensor used an internal Hall Effect sensor in order to keep the sensed current electrically isolated from the sensing circuit [27]. The current sensor output is an analog signal and, therefore, required conversion to a digital format. An Arduino Uno was used to read the current data during testing [28]. The Arduino Uno was connect to the central computer via a USB cable. Figure 47 illustrates the test circuit.
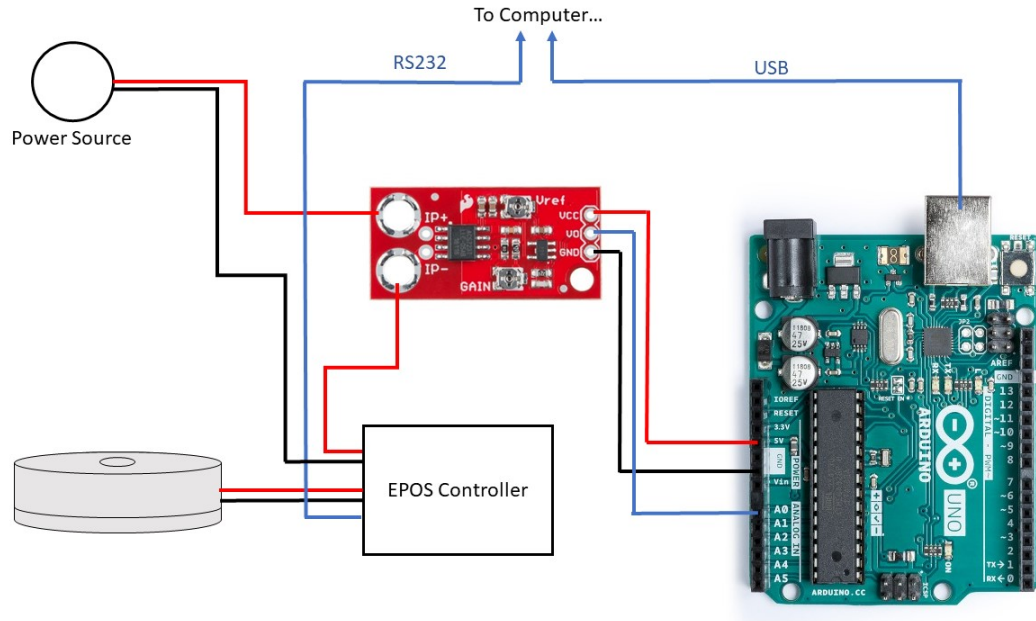
Figure 47.   Testbed Circuit Schematic

The central computer utilized a program written in LabVIEW software [29] to send rotation rate commands to the EPOS controllers that would, in turn, spin up or down the reaction wheels. LabVIEW is a graphical program for data acquisition and was used to create the block diagram pictured in Figure 48. In this block diagram, a connection is established with the EPOS controller with specified communications protocols. The EPOS controller velocity mode is selected, indicating that the sent commands are rotational velocity commands for the reaction wheels. From there, an initial command is sent to the EPOS controller and the code enters a "for-loop," represented as the box in Figure 48. The for-loop duration is defined by the commands in the upper left hand corner of Figure 48; these commands read in a *.txt* data sheet specified by the user containing a single reaction wheel's rotation rate profile. The reaction wheel rate file contains two column vectors, the command index number and the corresponding commanded speed in rpm. The commanded speed vector is a single reaction wheel's rotation rate for a given attitude maneuver, e.g., the MEEFT maneuver. One data point per 100 ms was specified. The LabVIEW program reads in the length of the command number vector and sets the for-loop to iterate an equivalent number of times. Within the for-loop, the current iteration number is displayed

for the user along with the current commanded speed that has been read from the reaction wheel rate document. That same commanded speed value is then sent to the EPOS controller. At this point, the for-loop waits a specified amount of time before executing the next iteration. The wait time is set to 100ms in Figure 48 to align with the sample times in the data files. When the for-loop is completed, the EPOS controller is commanded to zero the reaction wheel rate, the command connection severed, and the communication lines closed.
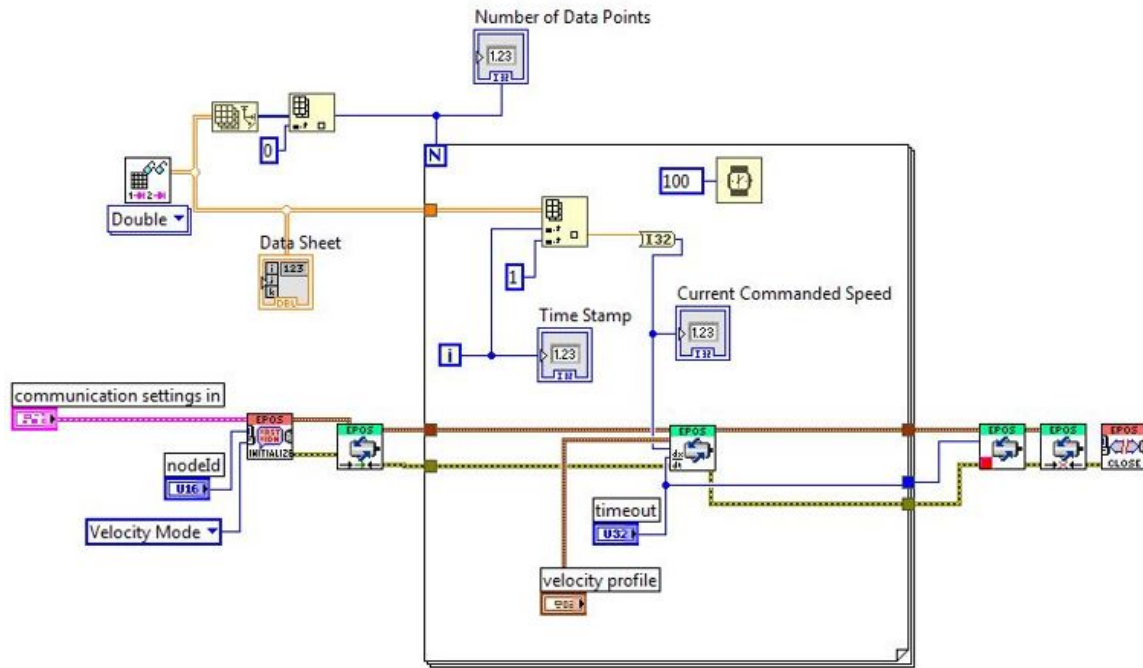
Figure 48.   LabVIEW Reaction Wheel Control Block Diagram

In order to read in and process the current sensor data, an Arduino code was adopted and edited from the Sparkfun website [30]. Within the Arduino code, hardware pin A0 is set as an analog-to-digital input. Each measurement is sampled 10 times and averaged before the output is reset to zero to calibrate the noise floor. The current sensor sensitivity value is set along with the reference voltage on the ACS723 board. For these tests, the sensitivity was set to $Sensitivity = 0.625$ and the voltage reference was $V_{ref} = 150mV$. The

current sensor sensitivity and reference voltage were set according to the instructions enumerated at [30] knowing small currents on the order of 10mA would need to be detected, which drives the sensitivity up. Moreover, only positive currents need to be measured, which allows the reference voltage to be set low. At this point, the Arduino opens the serial port with a baud rate of 9600 and begins to read the sensor voltage output every 2ms. The code takes the average voltage reading over the numbered samples that was set initially, i.e. 10 samples. The average voltage reading, V, is then converted into an equivalent current using the reference voltage and sensitivity values set earlier; this equation is represented as Equation (1.79).

$$i = (V - V_{ref}) * Sensitivity \qquad (1.79)$$

The current, i, is calculated in milliamps and the value is output via the serial monitor or serial plotter so that the data can be acquired for analysis.

With each hardware component identified and the data collection software explained, the test procedures were written in the following section in order to collect empirical electrical energy consumption data for the Eigenaxis, MEEFT, and EEERT maneuvers providing three maneuvers with which determine the power draw of the experimental momentum exchange attitude control system.

C.   TESTING PROCEDURES

First, the central computer is powered on and the LabVIEW code and Arduino code are opened. The Arduino Uno is connected and the Arduino code uploaded. Arduino's serial monitor is opened with the auto scroll function enabled. At this point, the power source is turned on and the EPOS controllers are powered up.

The LabVIEW code is run, pulling up the file explorer window within LabVIEW. After navigating to and highlighting the desired reaction wheel rotation rate profile, the Arduino serial monitor is cleared and the "OK" button on the file explorer window is clicked as quickly as possible. Swiftly starting the LabVIEW code after clearing the serial monitor is important in order to help flag the time when the maneuver started.

When the maneuver ends, the auto scroll function on the serial monitor is turned off, the last displayed value on the screen is close to the last recorded current reading from the attitude maneuver. The serial monitor output is copied from this point to the top and pasted into an Excel document to be read into MATLAB where it is processed for presentation.

D.   EMPIRICAL RESULTS AND ANALYSIS

With the testbed characteristics defined and the test procedures written, this section will present the power and energy data collected from running all four reaction wheel profiles for each of the three corner-case maneuvers. Running all three maneuvers on the testbed allows 12 unique reaction wheel power draw profiles to be tested, providing ample data to validate the used Equation (1.14) as a momentum exchange attitude control system's power draw model.

After running all four reaction wheel rotation rate profiles for the Eigenaxis solution, the current sensor data presented in Figure 49 was obtained. Figures 50 and 51 display the same collected power draw data for the MEEFT and EEERT maneuvers, respectively. Figures 49 through 51 are consistent with the predicted power profiles shown in Figures 40 through 42. The only discrepancy is a scale factor for the experimental system. This aspect will be discussed in greater detail later.

Figure 49 reasonably matches Figure 40 where the second reaction wheel draws the most power over the duration of the maneuver followed by the first reaction wheel, the third, and then the fourth. The power draws from Figure 49 are all constant throughout the coast phase of the Eigenaxis maneuver as was predicted in Figure 40. Similarly, Figure 50 shows the second reaction wheel drawing the most power over the maneuver following a parabolic path while the profiles and relative scale to the other three wheels reasonably match the power draws predicted in Figure 41. The same relation can be highlighted for Figures 42 and 51.
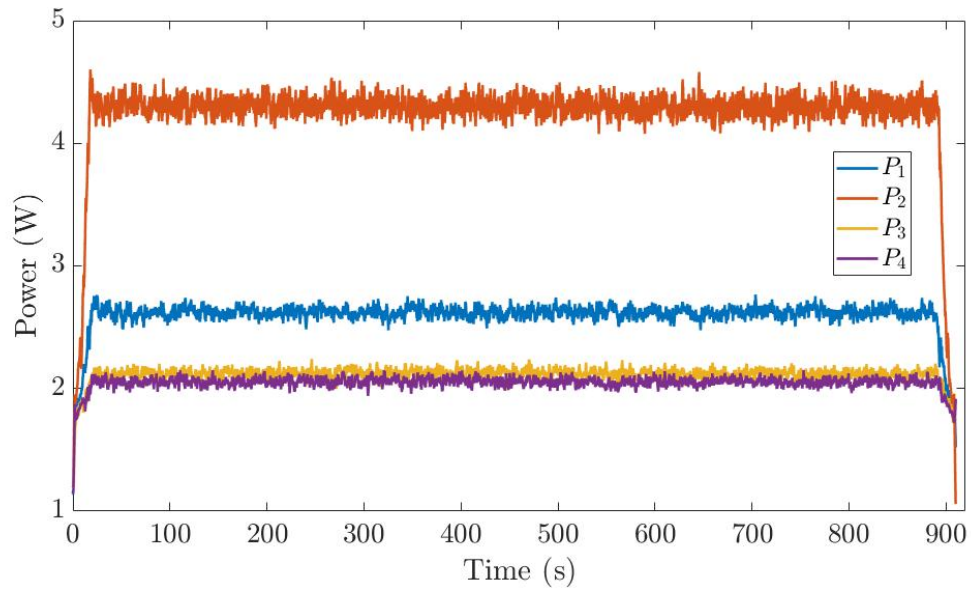
Figure 49.   Experimental Power Draw Data for Eigenaxis Maneuver
Matching Predicted Values of Figure 40
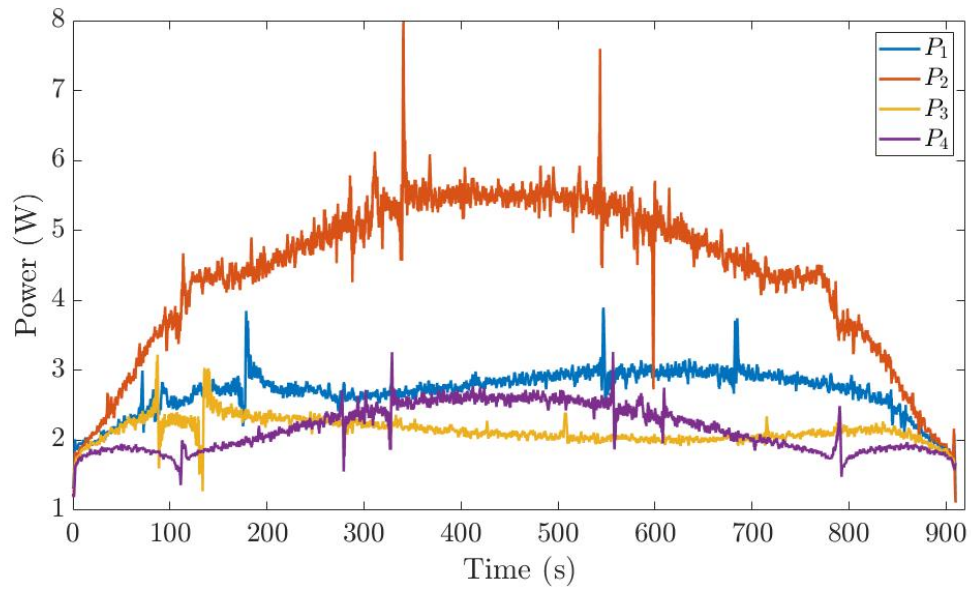
Figure 50.   Experimental Power Draw Data for Minimum Electrical
Energy, Fixed-Time Maneuver Matching Predicted Values of Figure 41
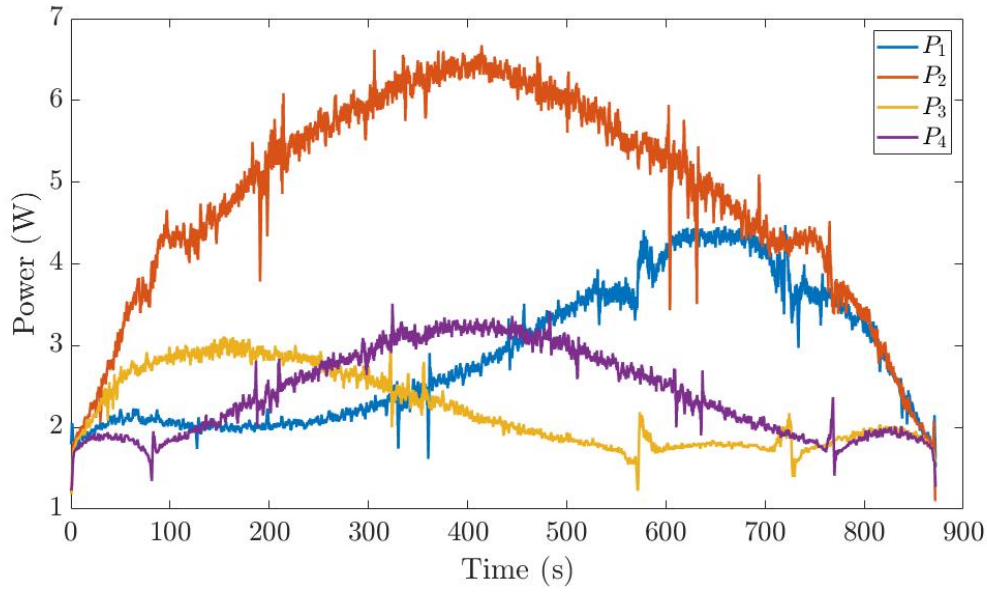
Figure 51.   Experimental Power Draw Data for Equivalent Electrical
Energy, Reduced Time Maneuver Matching Predicted Values of Figure 42

The scale difference between Figures 49, 50, and 51 compared to Figures 40, 41 and 42 is the result of an un-modeled quiescent current and four other potential factors. Powering both the reaction wheel controller and the reaction wheel draws a certain current even when the reaction wheel is not rotating. This power draw is not currently modeled in Equation (1.14) but could easily be incorporated if the quiescent current was measured and characterized. However, since the attitude control system is consistently powered throughout a spacecraft's life, the power required to sustain the attitude control system should not be part of the cost of any particular maneuver. Knowing this, the quiescent current term does not need to be incorporated into Equation (1.14) but rather should be measured and subtracted out of the collected data in order to correct the data's scale. In Figures 49 through 51, the quiescent current is large enough to shift the power draw of each maneuver up a little over 1 W. Considering this increase over an entire maneuver for all four wheels, the total consumed electrical energy for each maneuver will also be drastically larger than the predicted electrical energy consumption from Figures 43 through 45.

Even if the quiescent current was taken out of the collected power data, the scale of each wheel's power draw does not match the scale of each wheel's predicted power draw from Figures 40 through 42. This scale mismatch could be the result of four potential causes. The EPOS command nodes might scale up the reaction wheel's power draw, this is not accounted for in Equation (1.14). Second, Equation (1.14) does not account for motor efficiency, potentially causing the scale difference between the predicted and experimentally collected data. Third, the sensitivity setting on the current sensor might have been turned up too high, producing current data measurements higher than what was actually being drawn; this can be checked in the future by conducting additional calibration experiments. Lastly, the coefficient of viscous friction used throughout this thesis might not be accurate for this Maxon Motor reaction wheel system. If this value is different, the power draw scale could change significantly though the shapes of the curves would remain the same. The first possible error source might be due to an omitted power draw term for the specific motor control algorithm implemented in the command node in Equation (1.14). Because different command logic would draw power in different ways, the command node logic could simply be accounted for in Equation (1.14) to better predict the scale of the drawn power. The second possible error source would also be due to an omitted efficiency term within Equation (1.14). Since different motors have different efficiencies, the motor efficiency could also be accounted for in Equation (1.14). The last two potential sources of error do not have to do with the accuracy of Equation (1.14) as they are specific to the testbed used. Because the scale mismatch is a multiplier rather than an omission within Equation (1.14), the collected power data confirms that Equation (1.14) is indeed a reasonable power model for a real momentum exchange attitude control system.

To provide further confirmation that the collected power draw curves match the profiles of the model's predictions, each individual reaction wheel power profile in Figures 49, 50 and 51 were integrated and summed to produce Figures 52, 53, and 54, the total electrical energy consumption of the Eigenaxis, MEEFT, and EEERT maneuvers on the testbed. Each electrical energy consumption curves follows the same profile that was predicted in Figures 43, 44, and 45. The Eigenaxis maneuver consumes electrical energy in a linear fashion over the entirety of the coast period while rounding up and down during

the initial acceleration and final deceleration periods bookending the coast period. Both the MEEFT and EEERT maneuver electrical energy consumptions in Figures 44 and 45 followed by Figures 53 and 54 follow the path of half of a sine wave. The EEERT maneuver consumes a higher amount of energy in a shorter amount of time, however, and thus follows a steeper sine wave path than the MEEFT maneuver. The fact that the paths of Figures 52, 53, and Figure 54 match those predicted in Figures 43, 44, and 45 follows logically considering the experimentally collected power draw figures, Figures 49 through 51, matched the predicted power draw figures, Figures 40 through 42. It also follows logically that the consumed electrical energy scale was much larger than the predicted electrical energy consumptions due to the scaling differences of the corresponding power curves.
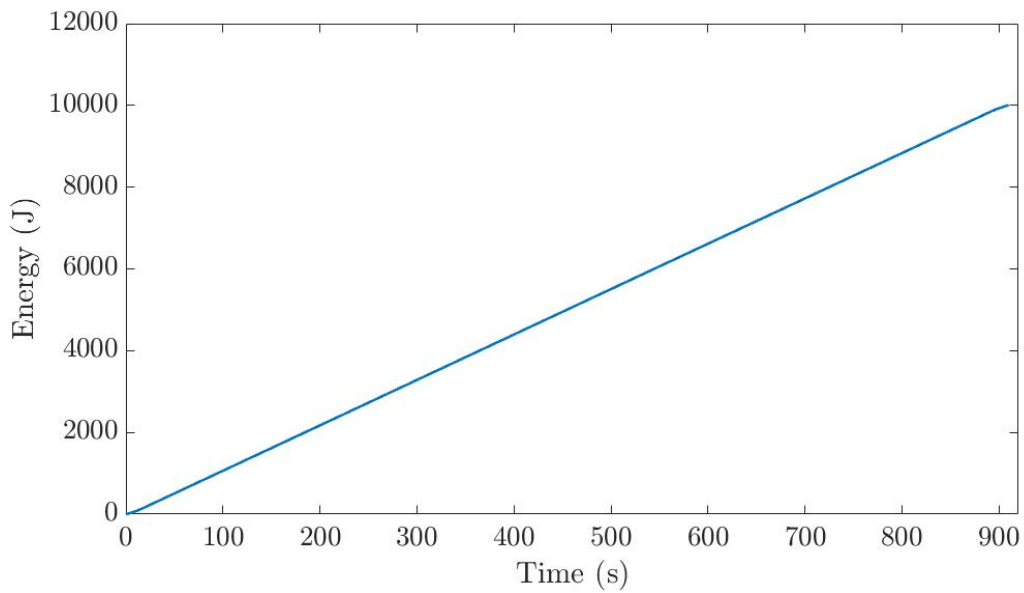
Figure 52.   Experimental Electrical Energy Consumption Data for
Eigenaxis Maneuver
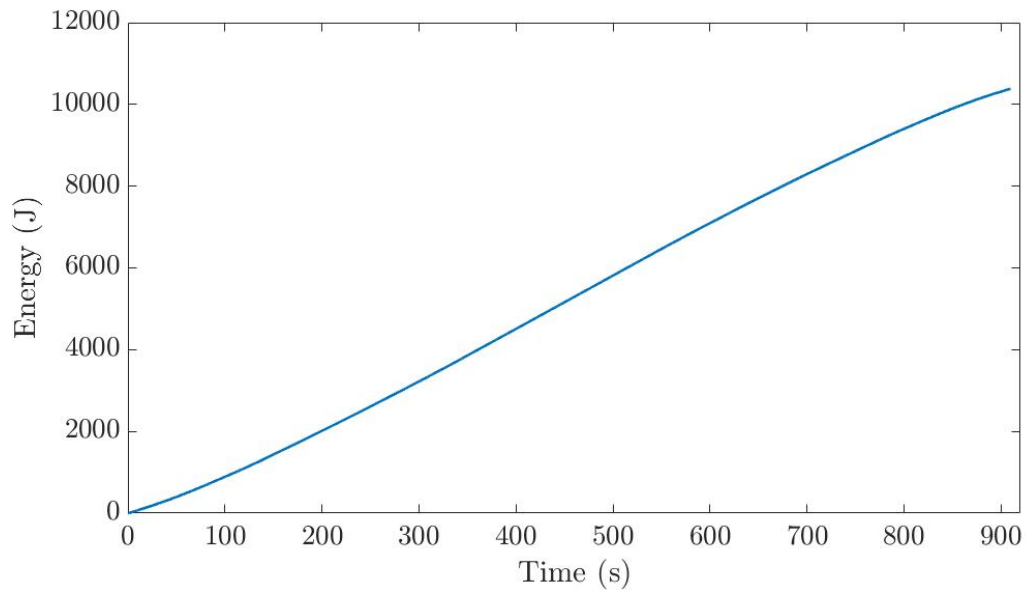
Figure 53.   Experimental Electrical Energy Consumption Data for
Minimum Electrical Energy, Fixed-Time Maneuver
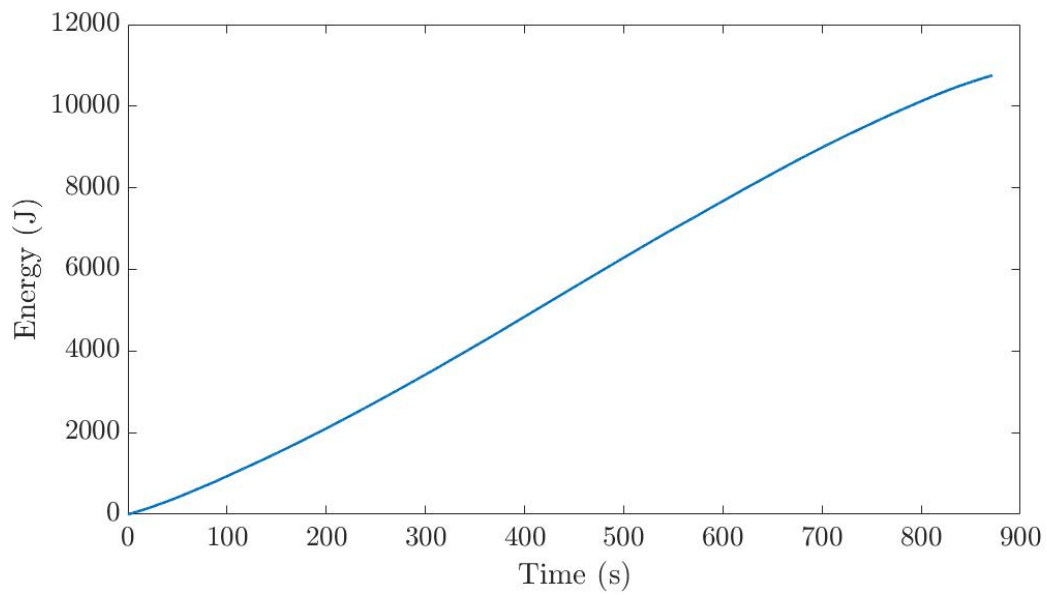
Figure 54.   Experimental Electrical Energy Consumption Data for
Equivalent Electrical Energy, Reduced Time Maneuver

The results of the experiments presented in this chapter provide evidence indicating

the momentum exchange attitude control system power model used as a cost function

within this thesis and in other published papers (such as [3] and [11]) does seem to correctly model such a system. The scales of the collected data differed from Equation (1.14) predictions but this scaling issue was attributed to a number of potential factors, none indicative that Equation (1.14) incorrectly models the power draw of a momentum exchange attitude control system.

THIS PAGE INTENTIONALLY LEFT BLANK

VII. SUMMARY AND CONCLUSION

When designing a spacecraft, operation duration as well as subsystem electrical energy consumption are critical aspects to be minimized in order to maximize the utility of the payload system. An attitude control system's electrical energy consumption and operation duration is wholly dependent on the desired attitude slew and the maneuver path taken to navigate between both attitudes. Although the Eigenaxis maneuver is industry standard, characterized by rotating a spacecraft the minimum distance between two attitudes, it is not always the shortest time maneuver nor the most energy efficient. This thesis was purposed to define a minimum time, minimum energy attitude slew operating envelope for a chosen spacecraft model via the application of optimal control theory. Once the operating envelope was established, an experiment to validate the accuracy of the momentum exchange attitude control system's power model used as the cost functional was conducted.

To create an operating envelope for the maneuver specifically studied within this research, the standard Eigenaxis maneuver was characterized to consume $E = 28.12J$ and $t_{slew} = 910.1s$. Chapter IV then built and solved a Minimum Electrical Energy, Fixed-Time maneuver, designed to consume less electrical energy while taking the same maneuver duration as the Eigenaxis maneuver. The resulting solution passed all of the identified necessary conditions and qualified for optimality; this optimal solution required $E = 18.35J$ and $t_{slew} = 910s$. Chapter V went to find an Equivalent Electrical Energy, Reduced Time maneuver in order to define the limits of the maneuver cost tradespace. To find this maneuver, the same problem formulation was used as to find the MEEFT maneuver with the exception of the final fixed time. After several iterations, the EEERT maneuver solution was found. The EEERT maneuver consumed $E = 28.12J$ and completed the maneuver within $t_{slew} = 872s$.

With all three corner-case trajectory costs found, a maneuver cost tradespace was created, fulfilling the first objective of this thesis. The tradespace, which demonstrated a nonlinear relationship between electrical energy consumption and maneuver duration,

illustrated that the Eigenaxis maneuver was the most expensive trajectory for the spacecraft to execute this particular maneuver. The tradespace doubles as an operating envelope, showing other maneuvers that minimize a single cost or a combination of costs exist. Thus, creating such an operating envelope for any particular spacecraft model and attitude maneuver would aid mission planners and spacecraft operators in greatly impacting the attitude control system's electrical energy consumption and additional payload mission time over the life of the spacecraft. To further justify the importance of the electrical energy – time tradespace, however, the electrical energy cost must accurately represent the measured maneuver cost. To provide this assurance, experiments were conducted to validate the power model, an analysis that has not been presented before.

These power model validation experiments were run on the Naval Postgraduate School's Control & Optimization Laboratory's attitude control system testbed. With the collected data, this thesis concluded that the power model does seem to correctly model the power draw of a real reaction wheel system. Validating the power model accomplished the second objective of this thesis.

To provide additional validation of the power model on larger reaction wheel attitude control systems, further tests on reaction wheels with rotational inertias acceptable for control of larger spacecraft should be completed. This is left as future work. Additionally, the electrical energy – time tradespace has only been identified for a single set of maneuver boundary conditions in this thesis. Due to the nonlinear relationship between electrical energy and time, similar trade plots should be developed for maneuvers about other axes. This is will fully characterize the space of electrical energy efficient maneuvers for the modeled spacecraft. This, too, is left as future work.

APPENDIX. ADDITIONAL NECESSARY CONDITIONS FOR THE MEEFT AND EEERT PROBLEMS

The Adjoint equations mentioned in Chapter IV are as follows:

$$\dot{\lambda}_{q_1} = -0.5(-\omega_3\lambda_{q_2} + \omega_2\lambda_{q_3} - \omega_1\lambda_{q_4})$$

$$\dot{\lambda}_{q_2} = -0.5(\omega_3\lambda_{q_1} - \omega_1\lambda_{q_3} - \omega_2\lambda_{q_4})$$

$$\dot{\lambda}_{q_3} = -0.5(-\omega_2\lambda_{q_1} + \omega_1\lambda_{q_2} - \omega_3\lambda_{q_4})$$

$$\dot{\lambda}_{q_4} = -0.5(\omega_1\lambda_{q_1} + \omega_2\lambda_{q_2} + \omega_3\lambda_{q_3})$$

$$-\lambda_{\omega_1} = 0.5(q_4\lambda_{q_1} + q_3\lambda_{q_2} - q_2\lambda_{q_3} - q_1\lambda_{q_4}) + \frac{\lambda_{\omega_2}}{J_2}(-J_3\omega_3 - J_w(Z_{31}\Omega_1 + Z_{32}\Omega_2 + Z_{33}\Omega_3 + Z_{34}\Omega_4) + J_1\omega_3)$$

$$+\frac{\lambda_{\omega_3}}{J_3}(-J_2\omega_2 - J_w(Z_{21}\Omega_1 + Z_{22}\Omega_2 + Z_{23}\Omega_3 + Z_{24}\Omega_4) + J_1\omega_2) + \mu_{\omega_1}$$

$$-\lambda_{\omega_2} = 0.5(-q_3\lambda_{q_1} + q_4\lambda_{q_2} + q_1\lambda_{q_3} - q_2\lambda_{q_4}) + \frac{\lambda_{\omega_1}}{J_1}(-J_3\omega_3 - J_w(Z_{31}\Omega_1 + Z_{32}\Omega_2 + Z_{33}\Omega_3 + Z_{34}\Omega_4) + J_2\omega_3)$$

$$+\frac{\lambda_{\omega_3}}{J_3}(J_1\omega_1 - J_w(Z_{11}\Omega_1 + Z_{12}\Omega_2 + Z_{13}\Omega_3 + Z_{14}\Omega_4) + J_2\omega_1) + \mu_{\omega_2}$$

$$-\lambda_{\omega_3} = 0.5(q_2\lambda_{q_1} - q_1\lambda_{q_2} + q_4\lambda_{q_3} - q_3\lambda_{q_4}) + \frac{\lambda_{\omega_1}}{J_1}(J_2\omega_2 + J_w(Z_{21}\Omega_1 + Z_{22}\Omega_2 + Z_{23}\Omega_3 + Z_{24}\Omega_4) - J_3\omega_2)$$

$$+\frac{\lambda_{\omega_2}}{J_2}(J_1\omega_1 + J_w(Z_{11}\Omega_1 + Z_{12}\Omega_2 + Z_{13}\Omega_3 + Z_{14}\Omega_4) - J_3\omega_1) + \mu_{\omega_3}$$

$$-\dot{\lambda}_{\Omega_1} = \frac{2R}{K_T^2}\beta\tau_1 + \frac{2R}{K_T^2}\beta^2\Omega_1 + 2\beta\,\Omega_1 + \frac{\lambda_{\omega_1}}{J_1}(-\omega_2 J_w Z_{31} + \omega_3 J_w Z_{21}) + \frac{\lambda_{\omega_2}}{J_2}(-\omega_1 J_w Z_{31} + \omega_3 J_w Z_{11})$$

$$+\frac{\lambda_{\omega_3}}{J_3}(-\omega_1 J_w Z_{21} + \omega_2 J_w Z_{11}) + \tau_1$$

$$-\dot{\lambda}_{\Omega_2} = \frac{2R}{K_T^2}\beta\tau_2 + \frac{2R}{K_T^2}\beta^2\Omega_2 + 2\beta\,\Omega_2 + \frac{\lambda_{\omega_1}}{J_1}(-\omega_2 J_w Z_{32} + \omega_3 J_w Z_{22}) + \frac{\lambda_{\omega_2}}{J_2}(-\omega_1 J_w Z_{32} + \omega_3 J_w Z_{12})$$

$$+\frac{\lambda_{\omega_3}}{J_3}(-\omega_1 J_w Z_{22} + \omega_2 J_w Z_{12}) + \tau_2$$

$$-\dot{\lambda}_{\Omega_3} = \frac{2R}{K_T^2}\beta\tau_3 + \frac{2R}{K_T^2}\beta^2\Omega_3 + 2\beta\,\Omega_3 + \frac{\lambda_{\omega_1}}{J_1}(-\omega_2 J_w Z_{33} + \omega_3 J_w Z_{23}) + \frac{\lambda_{\omega_2}}{J_2}(-\omega_1 J_w Z_{33} + \omega_3 J_w Z_{13})$$

$$+\frac{\lambda_{\omega_3}}{J_3}(-\omega_1 J_w Z_{23} + \omega_2 J_w Z_{13}) + \tau_3$$

$$-\dot{\lambda}_{\Omega_4} = \frac{2R}{K_T^2}\beta\tau_4 + \frac{2R}{K_T^2}\beta^2\Omega_4 + 2\beta\,\Omega_4 + \frac{\lambda_{\omega_1}}{J_1}(-\omega_2 J_w Z_{34} + \omega_3 J_w Z_{24}) + \frac{\lambda_{\omega_2}}{J_2}(-\omega_1 J_w Z_{34} + \omega_3 J_w Z_{14})$$

$$+\frac{\lambda_{\omega_3}}{J_3}(-\omega_1 J_w Z_{24} + \omega_2 J_w Z_{14}) + \tau_4$$

The Transversality conditions as discussed in Chapter IV are the following:

$$\lambda_{q_1}(t_f) = \nu_{q_1}$$

$$\lambda_{q_2}(t_f) = \nu_{q_2}$$

$$\lambda_{q_3}(t_f) = \nu_{q_3}$$

$$\lambda_{q_4}(t_f) = \nu_{q_4}$$

$$\lambda_{\omega_1}(t_f) = \nu_{\omega_1}$$

$$\lambda_{\omega_2}(t_f) = \nu_{\omega_2}$$

$$\lambda_{\omega_3}(t_f) = \nu_{\omega_3}$$

$$\lambda_{\Omega_1}(t_f) = \nu_{\Omega_1}$$

$$\lambda_{\Omega_2}(t_f) = \nu_{\Omega_2}$$

$$\lambda_{\Omega_3}(t_f) = \nu_{\Omega_3}$$

$$\lambda_{\Omega_4}(t_f) = \nu_{\Omega_4}$$

LIST OF REFERENCES

[1]   M. Karpenko, T. Lippman, I. Ross, J. Halverson, T. McClanahan, M. Barker, E. Mazarico, R. Besser, C. Dennehy, T. VanZwieten, A. Wolf, "Fast Attitude Maneuvers for the Lunar Reconnaissance Orbiter," presented at 42nd Annual AAS Guidance, Navigation, and Control Conference, Breckenridge, CO, January 31, 2019, Paper Number: AAS 19–053.

[2]   H. Marsh, M. Karpenko, Q. Gong, "Electrical-Power Constrained Attitude Steering," presented at AAS/AIAA Astrodynamic Specialists Conference, Stevenson, WA, August 20 to August 24, 2017, Paper number: AAS 17–774.

[3]   H. Marsh, M. Karpenko, Q. Gong, "Relationships Between Maneuver Time and Energy for Reaction Wheel Attitude Control." *Journal of Guidance, Control, and Dynamics,* vol. 41, no. 2, pp. 335–348, AIAA, Reston, VA: 2017.

[4]   I. M. Ross, *A Primer on Pontryagin's Principle in Optimal Control*. NY, USA: Collegiate Publishers, 2015.

[5]   K. Bilimoria, B. Wie. "Time-Optimal Three-Axis Reorientation of a Rigid Spacecraft." *Journal of Guidance, Control, and Dynamics,* vol. 16, no. 3, pp. 446–452, AIAA, Reston, VA: 1993

[6]   H. Shen, P. Tsiotras. "Time-Optimal Control of Asymmetric Rigid Spacecraft Using Two Controls." *Journal of Guidance, Control, and Dynamics,* vol. 22, no. 5, pp. 682–694, AIAA, Reston, VA: 1999

[7]   R. Proulx, I. Ross. "Time-Optimal Reorientation of Asymmetric Rigid Bodies." *Advances in the Astronautical Sciences*, vol. 109, pp. 1207–1227, AAS, Springfield, VA: 2001

[8]   B. Wie, *Space Vehicle Dynamics and Control*, 2nd ed. VA, USA: AIAA, 2008.

[9]   A. Fleming, P. Sekhavat, I. Ross, "Minimum-Time Reorientation of a Rigid Body." *Journal of Guidance, Control, and Dynamics,* vol. 33, no. 1, pp. 160–169, AIAA, Reston, VA: 2010.

[10]   S. Zhang, S. Qian, L. Zhang, "Optimal Control Techniques for Spacecraft Attitude Maneuvers," *ResearchGate*, 2011. [Online]. doi: 10.5772/14462.

[11]   M. Karpenko, C. J. Dennehy, H. C. Marsh, and Q. Gong, "Minimum Power Slews and the James Webb Space Telescope," presented at 27th AAS/AIAA Space Flight Mechanics Meeting, San Antonio, TX, February 5 to February 9 2017, Paper number: AAS 17–285.

[12]   H. Marsh, M. Karpenko, Q. Gong, "Energy Constrained Shortest Time Maneuvers for Reaction Wheel Satellites," presented at AIAA/AAS Astrodynamics Specialist Conference, Long Beach, CA, September 12 to September 15, 2016, AIAA Paper 2016–5579.

[13]   H. Marsh, "Optimally electrical energy slewing for reaction wheel spacecraft," Ph.D. dissertation, Applied Mathematics and Statistics, U. C. Santa Cruz, Santa Cruz, CA, 2018, [Online]. Available: https://escholarship.org/uc/item/75r6s251

[14]   "Lunar Reconnaissance Orbiter," 2019. Accessed: April 15, 2019. [Online]. Available: https://lunar.gsfc.nasa.gov/about.html

[15]   K. Hille, Ed. "LRO Mission Overview," *NASA,* 03-Aug-2017. Accessed: April 15, 2019. [Online]. Available: https://www.nasa.gov/mission_pages/LRO/overview/index.html

[16]   "Lunar Reconnaissance Orbiter," 2019. Accessed: April 15, 2019. [Online]. Available: https://lunar.gsfc.nasa.gov/images/223881main_LROconcept2_20080422_HI.jpg

[17]   Rob Garner, Ed., "LRO Spacecraft Instruments," *NASA*, 03-Aug-2017. Accessed: April 15, 2019. [Online]. Available: https://www.nasa.gov/mission_pages/LRO/spacecraft/index.html

[18]   T. Lippman, "Enhancing the Science Collection Capability of NASA's Lunar Reconnaissance Orbiter," M. S. thesis, Mech. Aero. Eng., NPS, Monterey, CA, 2017.

[19]   "Maxon Motors," *Maxon Motor AG.* Accessed April 30, 2019. [Online]. Available: https://www.maxonmotor.com/maxon/view/product/323772

[20]   B. Bialke, "High Fidelity Mathematical Modeling of Reaction Wheel Performance," presented at 21st Annual American Astronautical Society Guidance and Control Conference, 1998.

[21]   M. Karpenko, S. Bhatt, N. Bedrossian, I. Ross, "Flight Implementation of Shortest-Time Maneuvers for Imaging Satellites," *Journal of Guidance, Control, and Dynamics,* vol. 37, no. 4, pp. 1069–1079, AIAA, Reston, VA: 2014.

[22]   M. Karpenko, J. King, C. Dennehy, I. Ross, "Agility Analysis of the James Webb Space Telescope," *Journal of Guidance, Control, and Dynamics,* vol. 42, no. 4, pp. 810–821, AIAA, Reston, VA: 2019.

[23]   M. Karpenko, J. King, "Agility Envelopes for Reaction Wheel Spacecraft," presented at AIAA/AAS Astrodynamics Specialist Conference, Vail, CO, August 9 to August 13, 2015. [Online]. DOI: 10.1177/0954410018787866

[24]   Elissar Global, USA. 2017. DIDO, Software Package. ver. 7.5.5.

[25]   I. Ross, Q. Gong, M. Karpenko, R. Proulx. "Scaling and Balancing for High-Performance Computation of Optimal Controls," *Journal of Guidance, Control, and Dynamics,* vol. 41, no. 10, pp. 2086–2097, AIAA, Reston, VA: 2018.

[26]   "Maxon Motors," *Maxon Motor AG.* Accessed: April 30, 2019. [Online]. Available: https://www.maxonmotor.com/maxon/view/product/control/Positionierung/367676

[27]   "Current Sensor Breakout (ASC723) Hookup Guide," *Sparkfun*. Accessed April 30, 2019. [Online]. Available: https://learn.sparkfun.com/tutorials/current-sensor-breakout-acs723-hookup-guide?_ga=2.230522396.1816610114.1556687897-994826326.1540438863

[28]   "Arduino Uno Rev 3," *Arduino*. Accessed April 30, 2019. [Online]. Available: https://store.arduino.cc/usa/arduino-uno-rev3

[29]   National Instruments, USA. 2017. LabVIEW 2017, 32-bit.

[30]   G. Beckstein, USA. 2018. Sparkfun ASC712 and ASC723 Demo, ver. 2. [Online]. Available: https://learn.sparkfun.com/tutorials/current-sensor-breakout-acs723-hookup-guide?_ga=2.230522396.1816610114.1556687897-994826326.1540438863

THIS PAGE INTENTIONALLY LEFT BLANK

INITIAL DISTRIBUTION LIST

1.   Defense Technical Information Center
       Ft. Belvoir, Virginia

2.   Dudley Knox Library
       Naval Postgraduate School
       Monterey, California